

Contents lists available at ScienceDirect

Petroleum Science

journal homepage: www.keaipublishing.com/en/journals/petroleum-science



Original Paper

Investigation of interaction behavior between hydraulic fractures and gravels in heterogeneous glutenite using a grain-based discrete element method



Zhao-Peng Zhang a, *, Yu-Shi Zou b, Hai-Yan Zhu a, Shi-Cheng Zhang b

- ^a College of Energy (College of Modern Shale Gas Industry), Chengdu University of Technology, Chengdu, 610059, Sichuan, China
- b State Key Laboratory of Petroleum Resources and Engineering, China University of Petroleum (Beijing), Beijing, 102249, China

ARTICLE INFO

Article history: Received 7 April 2024 Received in revised form 14 August 2024 Accepted 15 August 2024 Available online 17 August 2024

Edited by Yan-Hua Sun

Keywords:

Hydraulic fracture propagation Fracture—gravel interaction behavior Grain-based discrete element method Glutenite

ABSTRACT

The glutenite reservoir is strongly heterogeneous due to the random distribution of gravels, making it challenging to perform hydraulic fracturing effectively. To solve this issue, it is essential to study interaction behavior between hydraulic fractures (HFs) and gravels. A coupled hydro-mechanical model is proposed for HF propagation in glutenite using a grain-based discrete element method. This paper first investigates the dynamic evolution of HFs in glutenite, then analyzes the influences of various factors such as horizontal stress difference ($\Delta \sigma$), minimum horizontal stress (σ_h), gravel content (V_g), gravel size (d_g) , and stiffness ratio of gravel to matrix (R_s) on HF propagation geometries. Results show that penetrating the gravel is the primary HF-gravel interaction behavior, which follows sequential and staggered initiation modes. Bypassing the gravel is the secondary behavior, which obeys the sequential initiation mode and occurs when the orientation of the gravel boundary is inclined to the maximum horizontal stress (o_H). An offset along the gravel boundary is usually formed while penetrating gravels, and the offsets may cause fracture widths to decrease by 37.8%-84.4%. Even if stress dominates the direction of HF propagation, HFs still tend to deflect within gravels. The deviation angle from $\sigma_{\rm H}$ decreases with rising $\Delta\sigma$ and increases with the increase of $d_{\rm g}$ and $R_{\rm S}$. Additionally, intra-gravel shear HFs (IGS-HFs) are prone to be generated in coarse-grained glutenite under high $\Delta \sigma$, while more gravel-bypassing shear HFs (GBS-HFs) tend to be created in argillaceous glutenite with high $R_{\rm S}$ than in sandy glutenite with low $R_{\rm S}$. The findings above prompt the emergence of a novel HF propagation pattern in glutenite, which helps to understand the real HF geometries and to provide theoretical guidance for treatments in the field. © 2024 The Authors. Publishing services by Elsevier B.V. on behalf of KeAi Communications Co. Ltd. This is an open access article under the CC BY-NC-ND license (http://creativecommons.org/licenses/by-nc-nd/ 4.0/).

Abbreviation

HF	Hydraulic fracture
GB	Gravel boundary
GB-HF	Gravel-bypassing HF
IG-HF	Intra-gravel HF
GBT-HF	Gravel-bypassing tensile HF
GBS-HF	Gravel-bypassing shear HF
IGT-HF	Intra-gravel tensile HF
IGS-HF	Intra-gravel shear HF

1. Introduction

Hydraulic fracturing technology has been applied to the development of oil and gas resources in tight glutenite reservoirs (Li et al., 2020; Zang et al., 2022). The glutenite formation is characterized by a strong heterogeneity owing to the presence of gravels of varying shapes and sizes. Previous studies (Liu et al., 2022a, 2022b) have suggested that the stiffness and strength of gravels may be 3–5 times larger than those of matrix. The significant mechanical contrast between the gravel and matrix can lead to complex interaction behavior between hydraulic fractures (HFs) and gravels. It has been widely believed that HFs are able to bypass (Li et al., 2013) or penetrate (Liu et al., 2019) the gravel, and may get arrested (Ma et al., 2017) or attracted (Huang et al., 2023) by gravels. However, the primary HF-gravel interaction behavior and

^{*} Corresponding author.

E-mail address: cdutzhangzp@126.com (Z.-P. Zhang).

underlying interaction mechanism remain unclear, making it hard to optimize the fracturing parameters for glutenite reservoirs with different in-situ stress states and gravel properties. Consequently, it is imperative to further understand the interaction mechanism between HFs and gravels to enhance the stimulation efficiency.

Numerous fracturing experiments have been conducted to investigate the interaction between HFs and gravels, and to qualitatively analyze the effects of geological and engineering factors on HF propagation geometries in glutenite (Wang J. et al., 2022; Liu et al., 2023; Zhang et al., 2023). It has been found that a bi-wing gravel-bypassing HF tends to be created in strongly-cemented glutenite with a low fraction of fine gravels under high $\Delta \sigma$; conversely, multiple tortuous gravel-bypassing HFs are inclined to be formed in weakly-cemented glutenite with a high fraction of large gravels under low $\Delta \sigma$ (Zou et al., 2021). Ma et al. (2017) concluded from pressure curves that injecting low-viscosity fracfluid at a low rate can result in narrow HFs, simultaneously with injection pressures fluctuating at high levels. Additionally, some fracture characterization technologies such as computed tomography (Liu et al., 2016) and acoustic emission monitoring (Shi et al., 2023) have been utilized to analyze the interaction behavior between HFs and gravels. It shows that branches are expected to form once the fracture tip encounters gravels and that the fracture width may decrease significantly where the HF starts to bypass the gravel. Furthermore, Nie et al. (2021) explored the influence of alternate loading on HF growth path in glutenite by changing the pumping rate periodically, stating that the gravel strength may be undermined due to the fatigue damage caused by alternate loading, thereby causing the HF to penetrate the gravel. Although these experiments have preliminarily studied the characteristics of HF propagation geometries in glutenite, they have yet to quantitatively reveal the interaction mechanism between HFs and gravels.

Numerical methods have been widely used in modelling the dynamic fracture propagation process, which is often difficult to acquire through experiments (Tang et al., 2024; Zhu et al., 2023; Zhao et al., 2021). Finite element method (FEM) and discrete element method (DEM) are two common and effective choices in simulating HF propagation in glutenite. To achieve accurate simulations of the fracture growth in glutenite, careful consideration must be given to the gravel generation and mechanical behavior of gravel boundaries (GBs). In FEM, meshes falling inside the gravel are grouped together to form a gravel-shaped area. Physical and mechanical properties of gravels are then assigned to the designated meshes in that area to represent gravels (Zhang and Wong, 2018). A hydro-mechanical-damage coupling scheme is often employed to characterize the interaction between the fracture tip and GB (Tang et al., 2022). Li et al. (2013) utilized the FEM-based rock failure process analysis (RFPA) software to successfully model the gravel-bypassing behavior of HFs and discovered the clustering phenomenon of micro-fractures at GBs. Similarly, Rui et al. (2018) used FEM to investigate the effects of gravel properties, matrix attributes, and interface cementation strength on multi-fracture propagation geometries in glutenite.

In contrast, the particle flow code (PFC) is a DEM-based numerical platform that is commonly applied to simulate meso-scale HF propagation in glutenite (Zhang et al., 2019; Huang et al., 2019) and crystalline rocks (Kong et al., 2021, 2022). In this method, the concept of clumps is adopted to generate gravels. Several separate balls are bonded together to create an assemblage that fits the real gravel shape (Zhang and Wong, 2018). Unlike the continuum mechanical method (e.g., FEM), mechanical behavior of materials is quantitatively represented by installing suitable contact models between two contacting balls in the PFC method (Potyondy and Cundall, 2004). In general, the parallel bond or flat-joint contact model is used to reflect the deformation of rocks. The differences in

mechanical properties among gravels, matrix, and interfaces are characterized by assigning different parameter values to the corresponding contacts. Zhang et al. (2019) established a PFC model for HF growth in glutenite with PBM and probed into the effects of the gravel strength and interface cementation properties on the interaction between HFs and gravels. Furthermore, Huang et al. (2023) used a novel soft bond contact model to depict the force—displacement law of balls inside the gravel and successfully gained the gravel-penetration geometry as observed in experiments.

In glutenite with high gravel content, gravels interlock and contact in a finite area (i.e., area contacting) along the GB (Li et al., 2020). However, most of the existing models focus on characterizing the irregular geometric shapes of gravels (Huang et al., 2023; Zhang et al., 2022) and the differences in mechanical properties between the gravel and matrix (Rui et al., 2018), ignoring the real contact pattern and interlocking behavior between gravels, which will lead to incorrect predictions for the interaction behavior between HFs and gravels. To fill this gap, this study adopts a grainbased discrete element method to generate gravels. This method has advantages in depicting the interlocking structure of minerals of crystalline rocks (Hofmann et al., 2015; Zhou et al., 2019) but is rarely used to characterize the contact features of gravels in glutenite. Moreover, despite extensive research on HF propagation geometries in glutenite, the primary interaction behavior between HFs and gravels and the underlying interaction mechanism still need to be better understood. In total, this paper aims to establish a hydro-mechanical coupling model for HF propagation in glutenite using the grain-based discrete element method and perform numerical simulations on PFC^{2D} platform to comprehensively understand the interaction mechanism between HFs and gravels. This article is organized as follows. Section 2 introduces the numerical methodology for HF propagation in the grain-based glutenite model. Section 3 presents the dynamic evolution process of HFs in glutenite, and analyzes the influences of stress states and gravel properties on the interaction behavior between HFs and gravels. Section 4 discusses the simulation results. Finally, the main conclusions are summarized in Section 5.

2. Numerical methodology

2.1. Gravel generation

In glutenite, it has been observed that gravels of irregular shapes are typically in contact with each other at finite areas along GBs, exhibiting the interlocking behavior (Li et al., 2020). To accurately represent the contact characteristics between gravels, a grain-based model was established through Voronoi tessellation (Fabjan et al., 2015) to randomly generate gravels, as shown in Fig. 1.

Firstly, a particle assembly was constructed by generating two groups of different sizes of balls (Fig. 1(a)). The center positions and sizes of balls in each group obeyed the uniform distribution. The larger white balls marked the gravel positions, and sizes and volume fractions of larger white balls were comparable to those of real gravels in glutenite. In contrary, the smaller gray balls represented the matrix in glutenite. Secondly, the centers of balls in contact were connected to form a network of polygons, as indicated with green lines in Fig. 1(b). Thirdly, a Voronoi polygon network could be obtained by linking the centroids (blue solid circles in Fig. 1(b)) of adjacent polygons, as indicated with blue lines in Fig. 1(b) and (c). The Voronoi polygons were classified into two groups: polygons covering the larger white balls were defined as gravel grains, and those covering the smaller gray balls were defined as matrix grains. Eventually, tiny particles with radii of 0.50–0.83 mm were created to fill the Voronoi polygon network (Fig. 1(d)). White particles

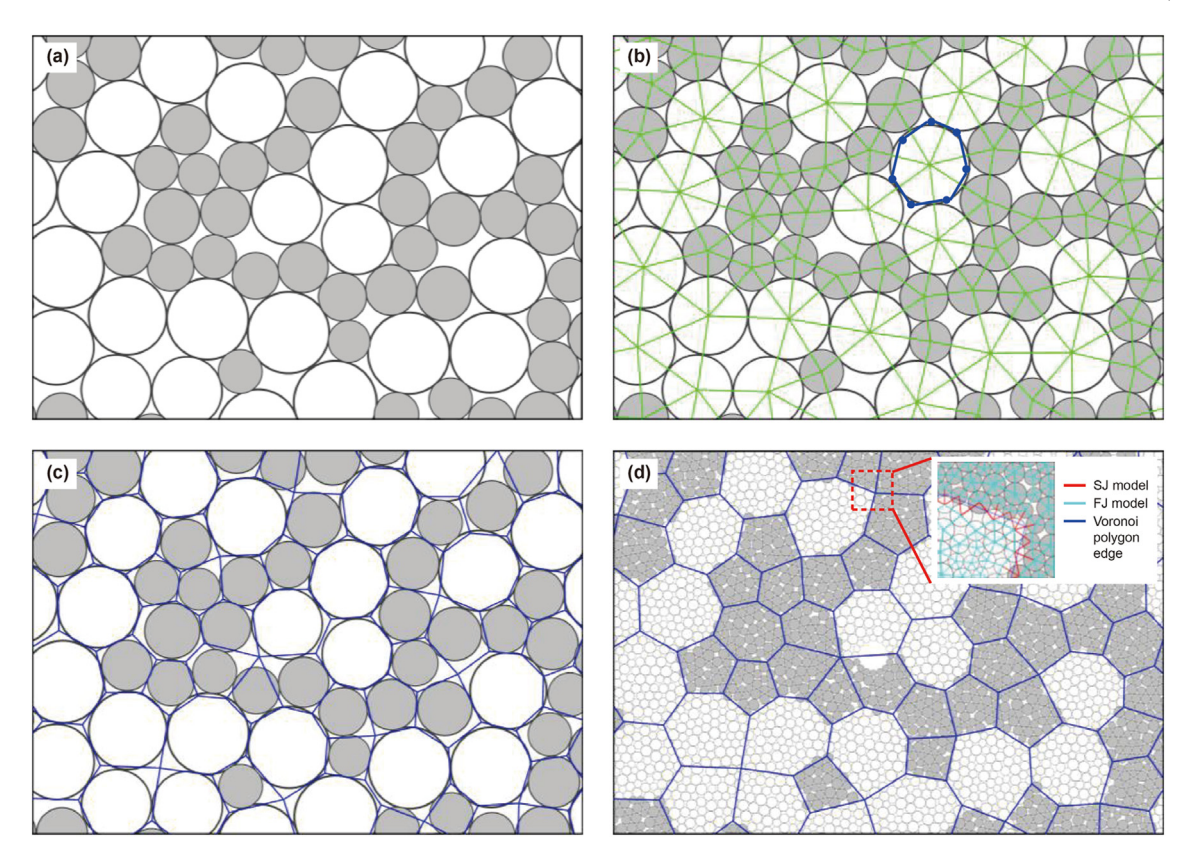


Fig. 1. Generation procedures of grain-based gravels. (a) Creating the particle assembly; (b) Forming the polygon network; (c) Forming the Voronoi polygon network; (d) Gaining grain-based gravels and assigning contact models.

falling into gravel grains gathered together to form grain-based gravels of various shapes. For the assignment of ball-ball contact models, the flat-joint (FJ) model (Potyondy, 2012) was installed at contacts entirely within the matrix or gravel polygons, while the smooth-joint (SJ) model (Ivars et al., 2008) was assigned to contacts intersecting the edges of gravel polygons, as shown in the subplot in Fig. 1(d). The FJ model described the deformation characteristics of gravels and matrix, and the SJ model characterized the opening or sliding of GBs.

A 100 mm \times 100 mm glutenite model (Fig. 2(a)) was established based on the four steps above to approximate the real glutenite (Fig. 2(b)) with $V_{\rm g}$ of 60% and $d_{\rm g}$ of 4–6 mm. Comparison between the model and real glutenite proves that the grain-based model gained by Voronoi tessellation is an effective method for characterizing the contact behavior of gravels. As a result, this study is to build the grain-based glutenite models with varying gravel sizes, contents, and strengths in the following sections. To facilitate the comparisons among different simulation cases, the default values of $V_{\rm g}$ and $d_{\rm g}$ are 60% and 10–12 mm, respectively, unless otherwise stated. Furthermore, a modelled wellbore with a diameter of 5 mm, consisting of sixteen balls with a diameter of 1 mm, was set at the center of the model domain.

2.2. Hydro-mechanical coupling scheme

The pore network model (Al-Busaidi et al., 2005; Potyondy, 2015; Shimizu et al., 2011; Wang T. et al., 2022; Yoon et al., 2014, 2015a, 2015b; Zhang et al., 2013) has been widely used in PFC^{2D} to achieve the coupling between solid deformation and fluid flow during HF propagation. In order to establish the pore network, all

ball centers in the system in Fig. 1(d) were connected, as indicated in blue lines in Fig. 3(a). Each polygon within this network represents a pore domain, which is assumed to be fully saturated with fluid at initial conditions to enhance computation efficiency. As shown in Fig. 3(b), each pore domain is adjacent to multiple other pore domains, and fluid exchange occurs if there is a pressure difference between the adjacent pore domains. To quantitatively calculate the fluid exchange volume, virtual flowing pipes were introduced and installed at the contact planes between two contacting balls, with the flowing pipe perpendicularly intersecting the edge between the two adjacent pore domains. Hence, the fluid is allowed to flow from the high-pressure pore domain to the low-pressure one through the flowing pipe. Please note that in the 2D model, the flowing pipe is typically a unit-thickness flat plate with finite length.

The volumetric flowing rate q_p through the pipe can be calculated by the cubic law (Eq. (1)) (Al-Busaidi et al., 2005)

$$q_{\rm p} = -\frac{w_{\rm p}^3}{12\mu} \frac{p_2 - p_1}{l_{\rm p}} \tag{1}$$

where w_p is the pipe width, m; l_p is the pipe length, m; p_2 and p_1 are fluid pressures of the pore domains which fluid flows out from and flows into, respectively; μ is the fluid viscosity, Pa s. l_p is usually calculated by $4r_1r_2/(r_1+r_2)$, in which r_1 and r_2 are radii of balls on both sides of the flowing pipe. w_p is related to the contact force and bond integrity, and is obtained by (Huang et al., 2019; Kong et al., 2021)

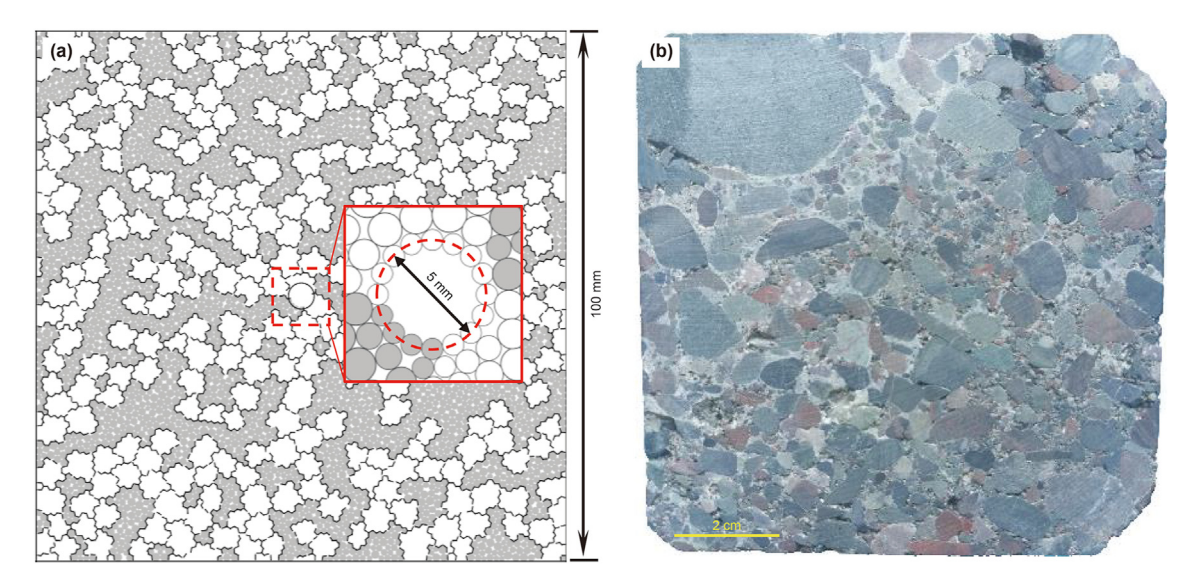


Fig. 2. Comparison between the model and real glutenite. (a) Glutenite model; (b) Real glutenite with interlocking gravels.

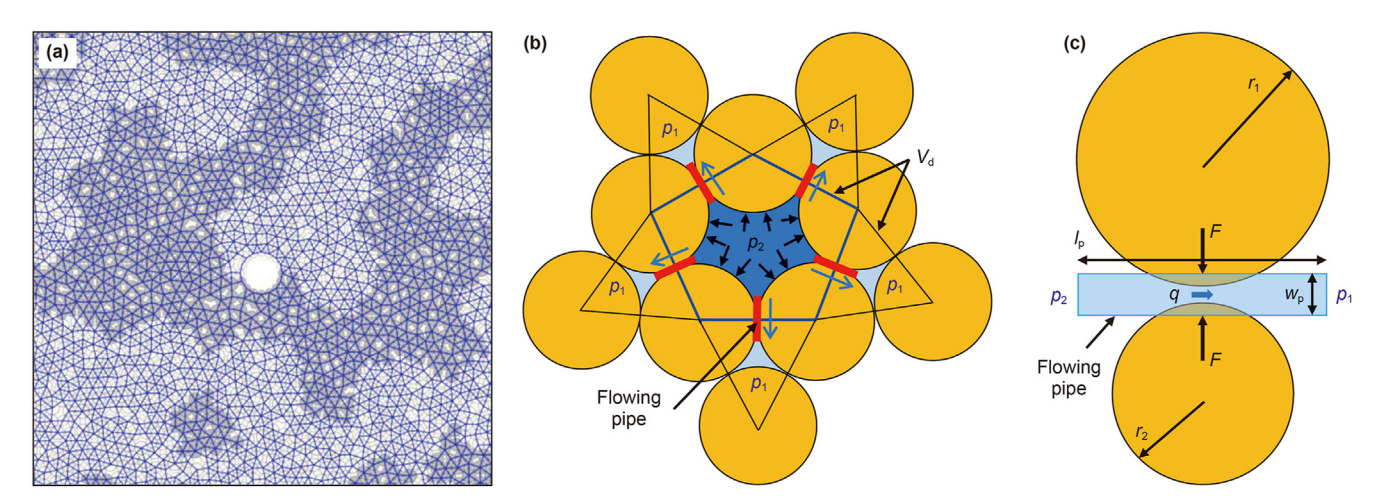


Fig. 3. Schematic of pore network model. (a) Network of pore domains; (b) Fluid exchange between the adjacent pore domains; (c) Flowing pipe between two contacting balls.

$$w_p = \frac{w_0 F_{n0}}{F_{n0} + |F_n|}$$
 (intact and compressive bond) (2.1)

$$w_{\rm p} = 2w_0 - \frac{w_0 F_{\rm n0}}{F_{\rm n0} + |F_{\rm n}|}$$
 (intact and tensile bond) (2.2)

$$w_p = \max(w_0, w_b + m\Delta w_d)$$
 (broken bond) (2.3)

where w_0 is the initial width, m; F_n is the normal contact force, N; F_{n0} is the normal contact force when w_p reduces to half of its initial value (i.e., $w_0/2$), N; w_b is the pipe width when the bond fails, m; m is the correction factor of the pipe width, dimensionless; Δw_d is the variation of the contact gap, m. When the bond is intact and under compression, w_p should be calculated by Eq. (2.1). If the bond is intact and under tension, w_p is supposed to be calculated by Eq. (2.2). When the bond is broken, w_p should be updated by Eq. (2.3).

Suppose that a pore domain connects other n pore domains through the flowing pipes, the variation of fluid volume (ΔV_f) in the core pore domain consists of the injection volume and inflow volumes from the n adjacent pore domains. In an iteration timestep Δt , ΔV_f is represented as (Al-Busaidi et al., 2005)

$$\Delta V_{\rm f} = \left(q_{\rm inj} + \sum_{i=1}^{n} q_{\rm p}^{(i)}\right) \Delta t \tag{3}$$

where $q_{\rm inj}$ is the injection rate, m³/s; $q_{\rm p}^{(i)}$ is the volumetric flowing rate through the *i*th flowing pipe, m³/s. The fluid pressure in a pore domain is affected by $\Delta V_{\rm f}$ and the variation of the real pore volume ($\Delta V_{\rm p}$). Thus, the fluid pressure variation (Δp) in a pore domain is calculated by (Al-Busaidi et al., 2005)

$$\Delta p = K_{\rm f} \frac{\Delta V_{\rm f} - \Delta V_{\rm p}}{V_{\rm p}} \tag{4}$$

where V_p is the real pore volume, m^3 , equal to $V_{d\phi}$ (V_d is the pore domain volume and ϕ is the porosity); K_f is the fluid bulk modulus, Pa. Δt should be carefully selected to ensure the stability of explicit iteration in PFC^{2D}. One of the necessary conditions for the numerical stability is that the pressure gradient direction of the natural seepage should remain unchanged after the fluid exchange between the core pore domain and n adjacent pore domains. In other words, the fluid pressure variation in the core pore domain during Δt should not exceed the minimum pressure difference between

the two ends of the flowing pipe connecting the core pore domain. According to Kong et al. (2021), Δt can be calculated by

$$\Delta t = \alpha_{t} \frac{V_{p}}{K_{f} \left(\sum_{i=1}^{n} \frac{\left(w_{p}^{(i)} \right)^{3}}{12\mu_{p}^{(i)}} \right)}$$
 (5)

where $w_p^{(i)}$ and $l_p^{(i)}$ are the width and length of the ith flowing pipe connecting the core pore domain, respectively, m; α_t is the safe factor ($\alpha_t < 1$). Compare Δt to the mechanical timestep Δt_m and take the less one as the final iteration timestep. Fig. 4 presents the workflow of sequential hydro-mechanical coupling for the HF propagation simulation in the PFC^{2D} model. It can be found that fluid flow and solid deformation modules proceeded alternately.

2.3. Micro-parameter calibration

The micro-parameters of the model mainly consist of the mechanical and seepage parameters. Because of the cross-scale issue, the microscopic mechanical parameters, primarily referring to the contact parameters, cannot be directly obtained from the macroscopic mechanical tests such as the tri-axial compression test and Brazilian splitting test. Consequently, the trial-and-error approach is frequently used in PFC to calibrate the values of microscopic mechanical parameters to accurately match the macroscopic mechanical behavior of real rocks. To minimize the number of trial-and-error attempts, the effective moduli of contacts within gravels and matrix were initialized based on the results of microindentation tests. Subsequently, the remaining contact parameters were determined by carrying out numerical simulations of triaxial compression tests and Brazilian splitting tests to match the experimental results. The values of microscopic mechanical

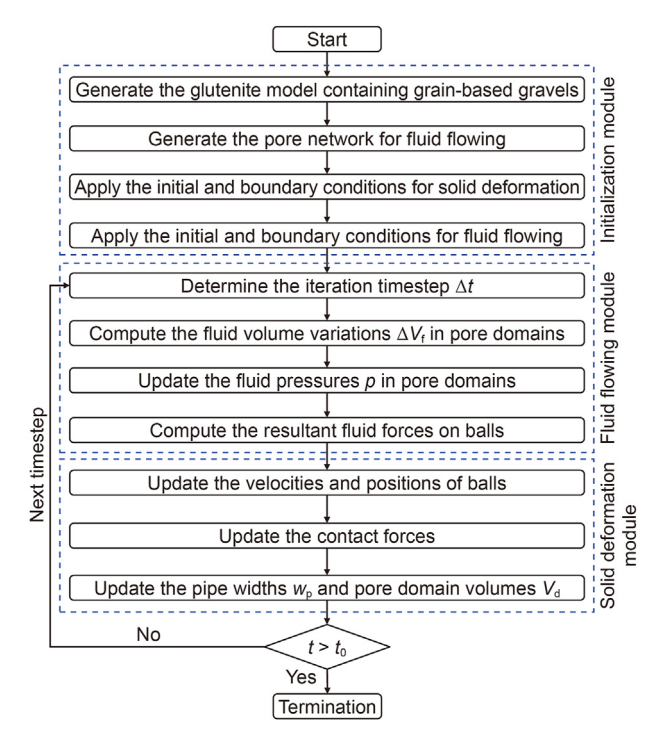


Fig. 4. Scheme of the sequential hydro-mechanical coupling for the HF propagation simulation in the PFC^{2D} model (t_0 is the simulation time required and this figure is corrected from Kong et al. (2021)).

parameters were calibrated against test results from Liu et al. (2022a) and are presented in Table 1.

Seepage parameters w_0 and m should be calibrated to approximate the actual attributes of fluid flowing in glutenite. The initial pipe width w_0 reflects the ability of fluid to percolate across the pore network and was calibrated by conducting numerical simulations of the permeability test (Kong et al., 2021). To begin with, a glutenite specimen with a diameter of 25 mm and a length of 50 mm (Fig. 5(a)) was generated using the method in Section 2.1, and a pore network (Fig. 5(b)) was created using the method in Section 2.2. Then, the fluid pressures in pore domains with a distance of ΔL away from the inlet were set to $p_{\rm in}$, and pressures in those with a distance of ΔL away from the outlet were set to p_{out} , creating a pressure difference to enable the fluid to flow across the numerical specimen. To save the simulation time, the fluid pressures in pore domains at $x \in (\Delta L, L - \Delta L)$ were preset by the linear distribution. The simulation did not cease until the inflow rate was almost equal to the outflow rate, attaining a steady flowing rate Q through the cross-section and dynamic equilibrium of fluid pressures.

Q is dependent on the specimen permeability and can be calculated based on Darcy's formula. Given that the glutenite permeability is 2×10^{-16} m², ΔL is 2.5 mm, μ is 1.0 mPa s, the fluid bulk modulus $K_{\rm f}$ is 2 GPa, $p_{\rm in}$ is 2 MPa, and $p_{\rm out}$ is zero, the theoretical value of Q is calculated to be 2.22×10^{-7} m³/s. The dynamic evolution of the inflow and outflow rates was calibrated through multiple adjustments of w_0 , and the results are presented in Fig. 5(c). It is indicated that the fluid pressures in the specimen almost reaches dynamic equilibrium when the iteration step is 15000–18000. During this range, the inflow rate is approximately identical to the outflow rate, and the pressure field presents the characteristic of linear distribution along the x-axis. When w_0 is set to 1.86×10^{-6} m, the numerical solution of the flowing rate in equilibrium is found to be 2.32×10^{-7} m³/s, which is close to the theoretical solution of 2.22×10^{-7} m³/s.

According to Kong et al. (2021), the correction factor m indicates the ability of the HF to deform under fluid pressures. It has been observed that the fracture stiffness tends to increase as m decreases. In this study, a 130 mm \times 130 mm ideal model consisting of 10201 regularly arranged balls with a diameter of 0.13 mm (Fig. 6(a)) was established to calibrate the value of m. To simulate the fracture width variation under fluid pressures, a pre-existing dry fracture with a length of 62.4 mm was installed at the center of the model. The tensile strengths of all contacts along the fracture were set to 0.1 Pa. Upon application of a constant fluid pressure to the fracture, the contacts along the fracture will fail easily, and the fracture width will gradually increase until the width distribution stabilizes. The numerical solution to the width distribution was validated against an analytical solution (Sneddon, 1946) to find the most appropriate value of m, which can reflect the actual deformation characteristics of the HF under fluid pressures. The analytical solution to the width distribution in an elastic solid is as follows.

$$w(x) = \frac{8(1 - v^2)p_{\rm f}}{\pi E} \sqrt{{L_0}^2 - x^2}$$
 (6)

where v is the Poisson's ratio, dimensionless; E is the Young's modulus, Pa; p_f is the constant fluid pressure in the fracture, Pa; L_0 is the half-length of the pre-existing fracture, m. Given that p_f is 2×10^6 Pa, L_0 is 0.0312 m, E is 22.0 GPa, and v is set to zero, the width distributions gained by the analytical solution and under different values of m are presented in Fig. 6(b). It is found that the fracture width at the same x-coordinate increases with m, and the numerical solution to the width distribution is consistent with the

Table 1The calibrated values of microscopic mechanical parameters.

Ball parameters Minimum ball radius r_{\min} , mm Ratio of the maximum to minimum ball radius r_{\max}/r_{\min} Ball density ρ , kg/m³		0.5 1.66 2750
Contact parameters within gravels and matrix		
	Gravel	Matrix
Total number of elements $N_{\rm r}$	4	4
Effective modulus E*, GPa	42	21
Normal-to-shear stiffness ratio κ*	1.6	1.6
Tensile strength $\sigma_{\rm c}$, MPa	12	9
Cohesion c, MPa	50	35
Friction angle ϕ , $^{\circ}$	60	45
Friction coefficient η	0.3	0.3
Contact parameters at interfaces		
	Gravel-gravel interface	Gravel-matrix interface
Normal stiffness k_n , GPa/m	24000	18000
Shear stiffness k_s , GPa/m	12000	9000
Joint tensile strength σ_{ci} , MPa	6	6
Joint cohesion c _i , MPa	23	23
Joint friction angle ϕ_{i} , $^{\circ}$	60	60
Joint friction coefficient $\eta_{\rm j}$	0.3	0.3

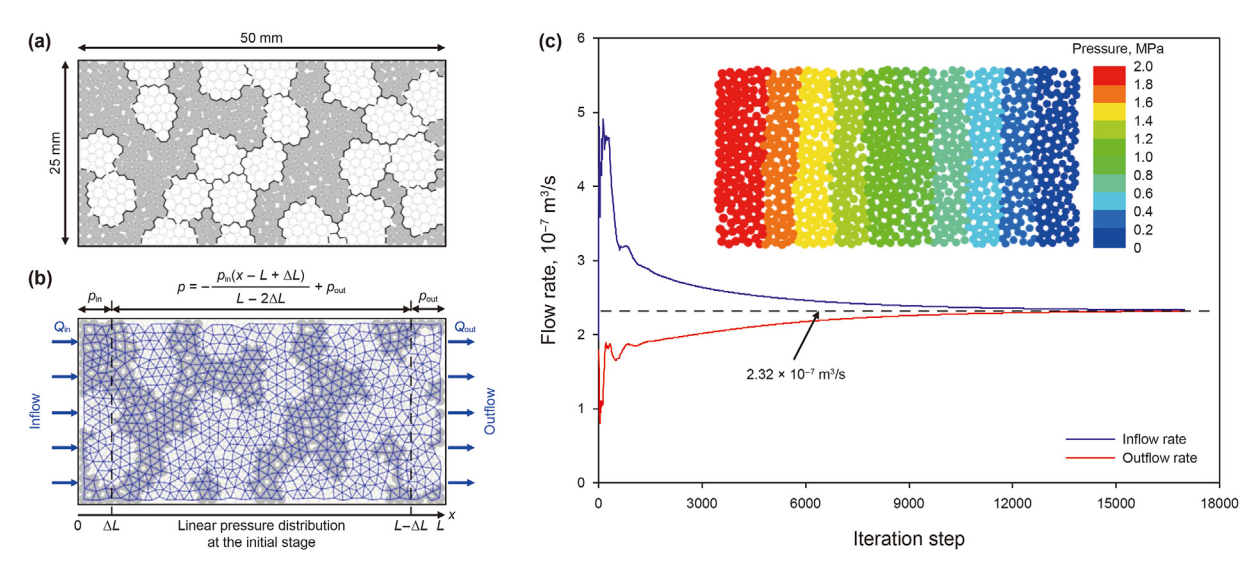


Fig. 5. The calibration of the initial pipe width w_0 . (a) The modelling glutenite specimen for the permeability test; (b) The initialization of the pore network; (c) The variation curve of the inflow and outflow rates versus the iteration step.

analytical solution when m is 0.4. Table 2 lists the values of the initial pipe width w_0 , correction factor m, and other relevant fluid properties. These parameters stay the same in the following numerical simulations.

In terms of the configuration of in-situ stresses, the contrast coefficient K_h of horizontal stresses (as defined in Eq. (7)) was introduced to assess the relative magnitude of the maximum and minimum horizontal principal stresses (Beugelsdijk et al., 2000).

$$K_{h} = \frac{\sigma_{H} - \sigma_{h}}{\sigma_{h}} \tag{7}$$

where $\sigma_{\rm H}$ and $\sigma_{\rm h}$ are the maximum and minimum horizontal principal stresses, respectively, MPa. If $\sigma_{\rm h}$ and $\sigma_{\rm H}$ are set to 30 and 39 MPa, respectively, $K_{\rm h}$ is 0.3. To facilitate the comparisons among different simulation cases, the default values of $\sigma_{\rm h}$ and $\sigma_{\rm H}$ are 30 and 39 MPa, respectively, unless otherwise stated. Additionally, the frac-fluid is injected into the wellbore at a rate of 5 × 10⁻⁵ m³/s.

3. Simulation results

3.1. Dynamic evolution characteristics of hydraulic fractures in glutenite

A benchmark case was conducted to elucidate the dynamic evolution characteristics of HFs in glutenite. It should be noted that the gravel content was considered as 68% in this case.

3.1.1. Asynchronous initiation

Figs. 7 and 8 show the HF initiation geometries at the wellbore wall in glutenite. The wellbore is located at the GB, with the right half of the wellbore wall consisting of gravel particles 1 to 8, and the left half of the wellbore wall consisting of matrix particles 9 to 16. The interface between the gravel and matrix at the wellbore wall is between particles 1 and 16, and between particles 8 and 9. Results reveal that the left and right wings of the HF initiate asynchronously at the wellbore. It is observed that at iteration step 3051, the

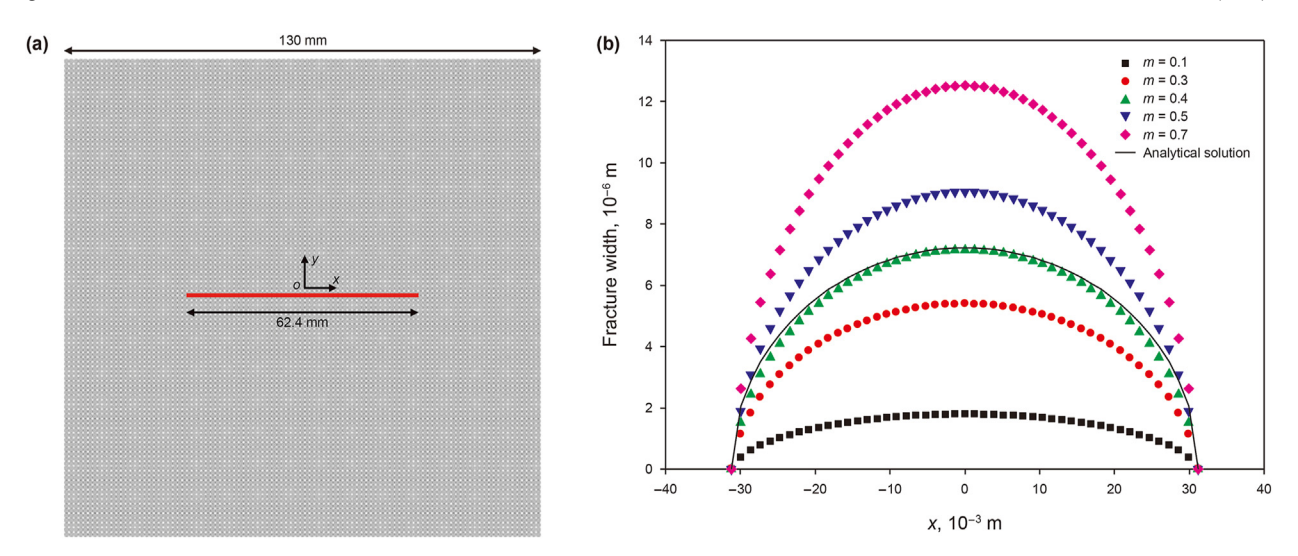


Fig. 6. The calibration of the correction factor m. (a) The numerical model containing a pre-existing fracture in the center; (b) The distributions of the fracture width obtained by the analytical solution and under different values of m.

Table 2The values of the seepage parameters and fluid properties.

Initial pipe width w_0 , m	Correction factor m	Fluid viscosity μ , mPa s	Fluid bulk modulus $K_{\rm f}$, GPa
1.86×10^{-6}	0.4	1.0	2.0

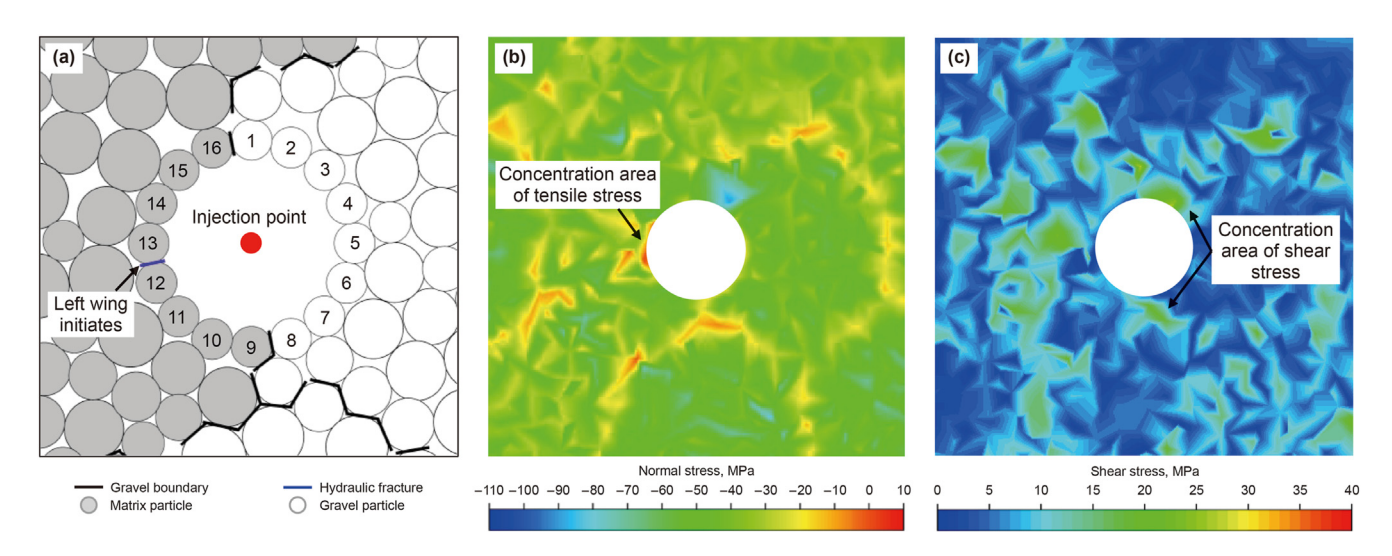


Fig. 7. Initiation geometry of the left-wing fracture and stress distribution near the wellbore at iteration step 3051. (a) Fracture geometry; (b) Normal stress distribution; (c) Shear stress distribution.

contact between particles 12 and 13 is fractured, and the left wing of the HF initiates on the matrix side of the wellbore (Fig. 7(a)). By injecting the frac-fluid continuously, the left wing keeps propagating, and two more fractures are created before the right wing initiates. It is not until iteration step 4210 that the contact between particles 4 and 5 fails, and the right wing of the HF initiates on the gravel side of the wellbore (Fig. 8(a)).

In combination with the interpolated normal stress distribution indicated in Fig. 7(b), it can be seen that there is a concentration area of tensile stress in the matrix on the left of the wellbore at iteration step 3051, and the local tensile stress within this area is higher than the tensile strength of matrix (9 MPa). However, the area within the gravel on the right of the wellbore is still under

compression, with the compressive normal stress approximately 40–50 MPa. Fig. 8(b) further illustrates that at iteration step 4210, a concentration area of tensile stress appears in the gravel on the right of the wellbore, and the local tensile stress within that area is higher than the tensile strength of gravels (12 MPa), making the gravel to fail. It demonstrates that the asynchronous initiation of the left and right wings may be attributed to the difference in mechanical properties between the gravel and matrix. As shown in Table 1, the stiffness of the matrix is lower than that of the gravel, which leads to a relatively larger normal displacement between particles at the two ends of the matrix contact than the gravel contact under the same wellbore pressure. This, in turn, makes it easier for the matrix side of the wellbore to form a concentration

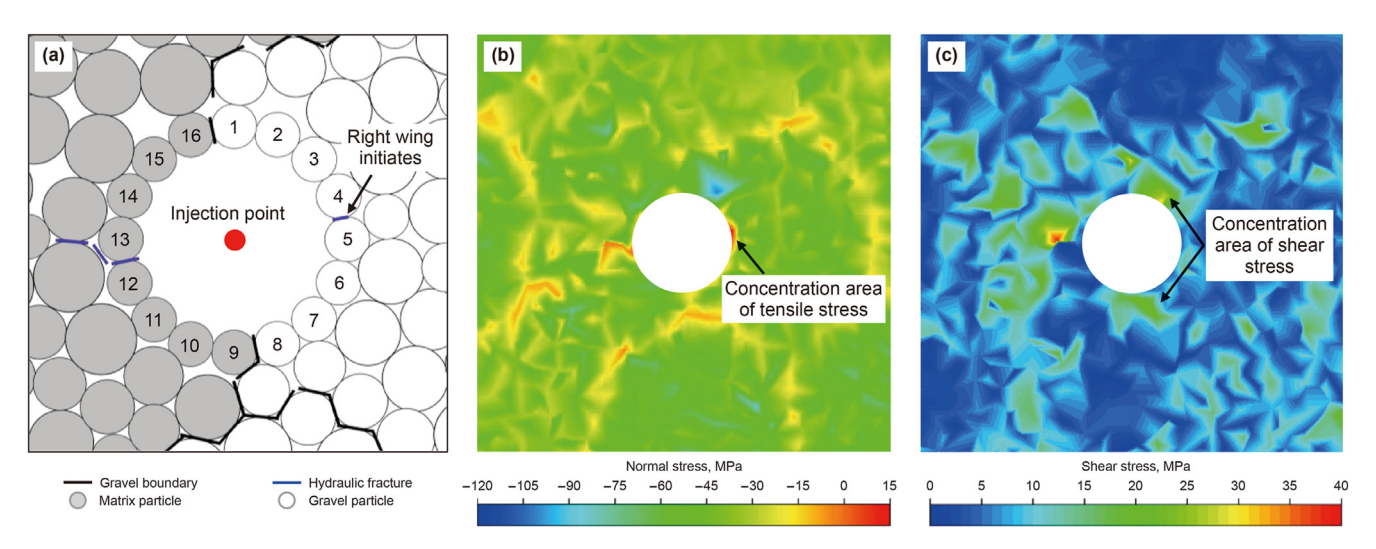


Fig. 8. Initiation geometry of the right-wing fracture and stress distribution near the wellbore at iteration step 4210. (a) Fracture geometry; (b) Normal stress distribution; (c) Shear stress distribution.

area of tensile stress. Furthermore, the tensile strength of the matrix is also lower than that of the gravel, causing the matrix contact to reach the tensile failure strength earlier than the gravel contact.

It is found that the HFs initiate nearly in the direction of $\sigma_{\rm H}$. Some scholars (Yu et al., 2021; Ma et al., 2017) suggest that HFs may initiate at GBs if gravels exist near the wellbore. In this case, the GBs between particles 1 and 16 and particles 8 and 9 remain intact, mainly due to the orientations of these interfaces being inclined to the direction of $\sigma_{\rm h}$, causing the GBs to be compressed by $\sigma_{\rm H}$. It is worth noting that there are concentration areas of shear stress near the GBs at iteration step 3051 (Fig. 7(c)). These areas keep expanding as the fluid is injected continuously, according to Fig. 8(c), suggesting that the GBs is likely to fail due to the interface slippage under shear stress.

3.1.2. Interaction behavior between hydraulic fractures and gravels Fig. 9(a) displays the global propagation geometries of HFs in the benchmark case. It is indicated that the HF penetrates or bypasses the gravel after the fracture tip encounters the GB. The left wing of the HF penetrates gravels G1 and G2, while the right wing

penetrates gravels G3, G4, and G5 successively. Additionally, the left wing bypasses the gravel along the interface between gravels G8 and G9 in area B1, while the right wing propagates along the GB between gravels G10 and G11 in area B2. The experimental results (see Fig. 2(b)) of hydraulic fracturing in glutenite by Zou et al. (2021) are used to validate the HF propagation geometries in the benchmark case. It is noted that the fracturing experiment was conducted under conditions similar to the benchmark case. Fig. 2(b) presents the HF propagation geometry in the computed tomography scanning graph transverse to the wellbore. According to Fig. 2(b), the left wing crosses gravels consecutively, while the right wing penetrates gravels in the near-wellbore area but bypasses gravels as it approaches the specimen boundary. It is observed that the numerical results of the HF propagation geometry in Fig. 2(a) are in good agreement with the experimental results, demonstrating that the model for predicting HF propagation geometries in glutenite is reliable.

Fig. 9(a) indicates that the HF crosses the GB from the matrix to the interior of the gravel at locations C1, C3, and C6, and from the gravel to the matrix at locations C2 and C5. Additionally, the HF

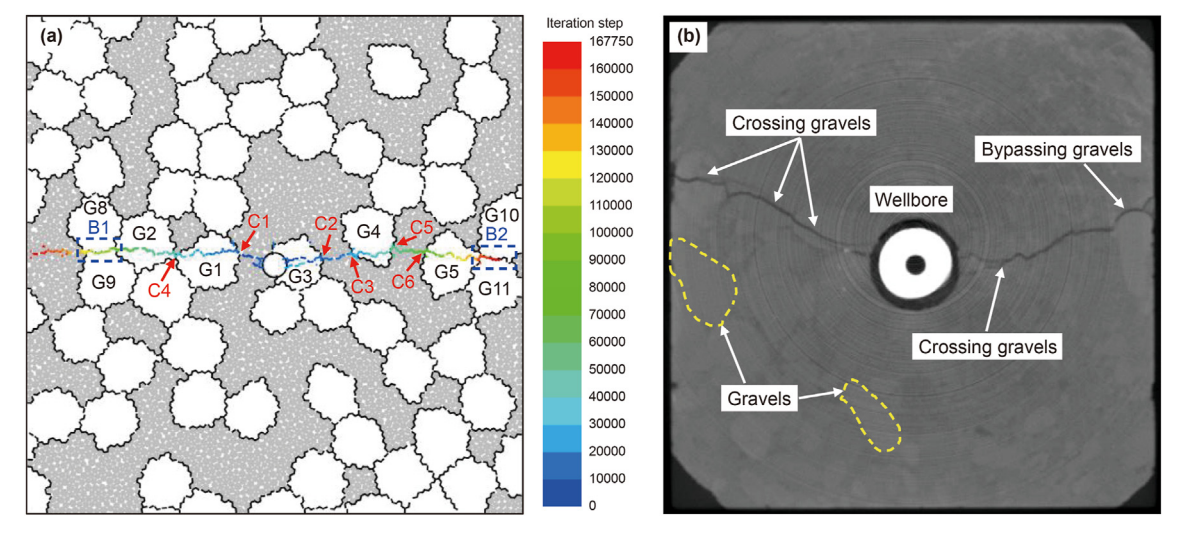


Fig. 9. The global fracture propagation geometry. (a) Numerical results of the benchmark case; (b) Experimental results from Zou et al. (2021). The color bar on the right denotes the iteration step at which the local grain-scale fracture was created.

crosses over the interface between gravels G1 and G2 directly at location C4. Fig. 10 presents a visual representation of the fracture propagation sequence for crossing GBs at locations C1 to C6 based on the iteration step (t) at which the local grain-scale fracture was formed. Fig. 10(a)-(c), and (f) suggest that penetrating into the gravel from the matrix follows a sequential initiation mode. Firstly. the GB is opened or sheared when the fracture intersects with it. Subsequently, the HF diverts toward and propagates along the GB. Finally, the HF diverts again into the interior of the gravel at a mechanically weak spot on the interface. For example, at location C1 (Fig. 10(a)), a gravel-bypassing shear HF (GBS-HF) is first created at t = 12331 once the fracture meets the gravel, then an intra-gravel tensile HF (IGT-HF) is generated near the boundary at t = 12398. The HF just propagates a short distance along the GB before diverting into the gravel, with only one or two interface contacts failing. This can be attributed to the heterogeneous orientations of interface contacts intersecting with GBs. The orientations of some interface contacts are almost inclined to the direction of σ_h . Compared to diverting into the gravel, more energy is needed to overcome the compression by σ_H to break the interface contacts if the HF propagates a long distance along the GB.

Fig. 10(b) and (e) show that crossing the GB from the gravel into the matrix follows a staggered initiation mode. In other words, the matrix in front of the fracture tip fails first upon the HF intersecting with the GB. As the fluid pressure at the fracture tip increases, the GB is fractured, leading to communication between the preexisting fracture and fracture tip. For instance, around location C2, a tensile HF is created first in the matrix at t = 16248 before the fracture crosses the GB, followed by the initiation of a GBS-HF on the interface at t = 16690 to communicate with the isolated fracture formed previously, as presented in Fig. 10(b). The fracture generated before the failure of the GB is referred to as a "drv" fracture, in which no fluid is present due to the separation from the primary fracture. This propagation behavior observed in this study is consistent with the experimental results obtained by using realtime photography and acoustic emission monitoring methods. Some scholars observed the identical initiation mode in their investigations into the hydraulic micro-cracking behavior in crystalline rocks (Kong et al., 2021; Isaka et al., 2019; Chen et al., 2015). They suggest that the staggered propagation behavior may result from the induced stress intensity around the fracture tip and local heterogeneity.

Moreover, it is found from Fig. 10(d) that the HF can pass through the interface between two adjacent gravels. At location C4, a gravel-bypassing tensile HF (GBT-HF) initiates first on the boundary of gravel G1 at t = 40767, when the fracture tip arrives at the interface. Afterward, another GBT-HF is formed on the boundary of gravel G2 at t = 44257. Further, the HF penetrates the GB, generating an IGT-HF within gravel G2 at t = 44374, and transiting the fracture growth trajectory from gravel G1 into the adjacent gravel G2. Notably, the behavior of the HF crossing the interface between two adjacent gravels obeys the sequential initiation mode.

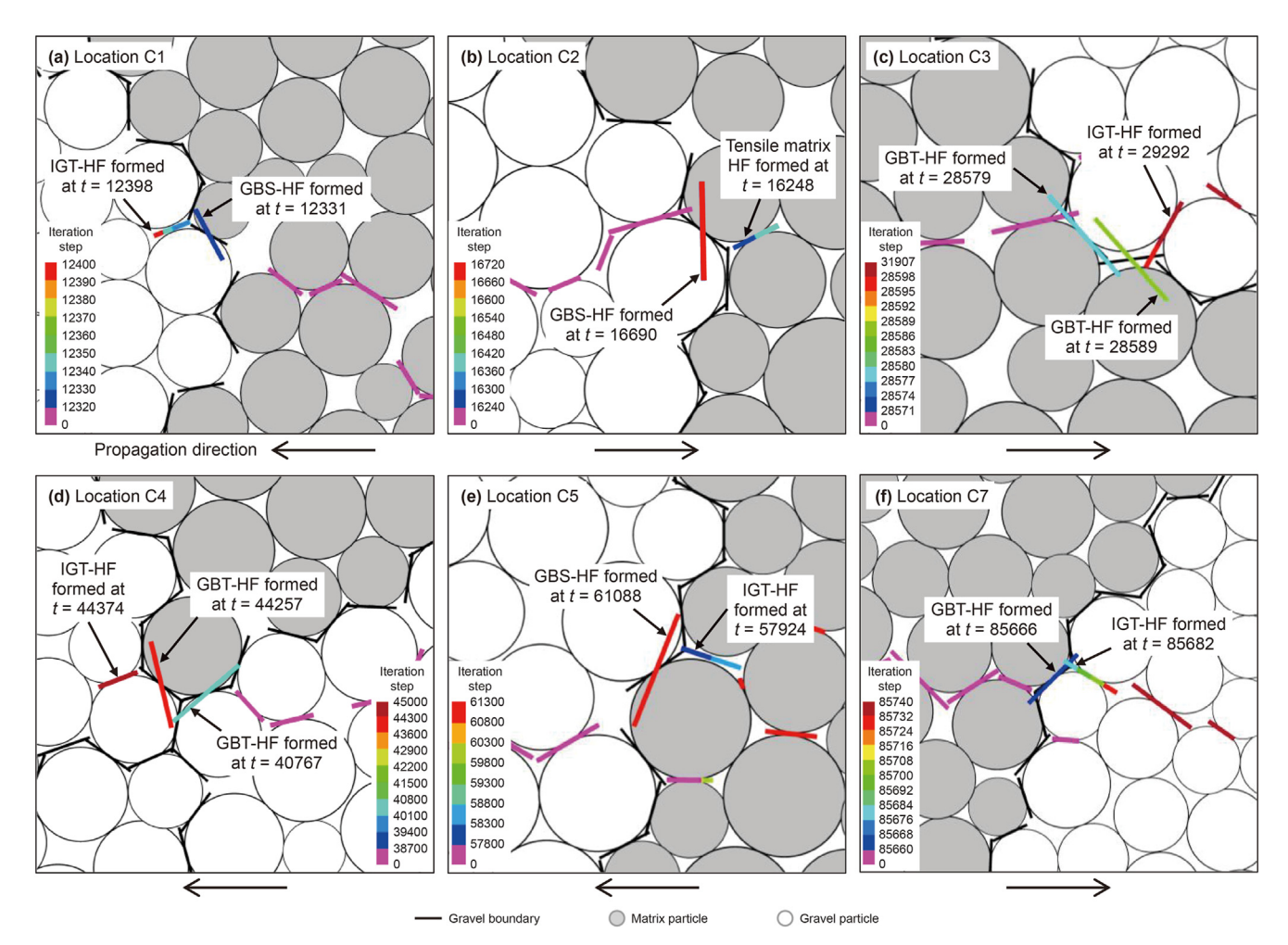


Fig. 10. The dynamic evolution process of the HF crossing the GB at different locations. (a) to (f) illustrate the fracture propagation paths at locations C1 to C6, respectively.

As shown in Fig. 9(a), the left wing bypasses the gravel along the interface between gravels G8 and G9 in area B1, while the right wing grows along the GB between gravels G10 and G11 in area B2. The dynamic evolution of the growth trajectory for bypassing gravels is presented in Fig. 11. In area B1 (Fig. 11(a)), it can be seen that a GBT-HF first initiates on the boundary at t = 92479 after the left wing encounters gravel G9. This is followed by the generation of another GBT-HF at t = 95123, causing the HF to divert and propagate along the interface between two contacting gravels. Subsequently, multiple GBT-HFs are formed during growing along the GB. For the right wing (Fig. 11(b)), a similar bypassing behavior can be found in area B2. It is noteworthy that the behavior of bypassing gravels follows the sequential initiation mode, without generation of "dry" fractures near the fracture tip. Further exploration of the mechanism behind the sequential and staggered initiation modes will be conducted in combination with the cloud map of stress around the fracture tip in the following section.

3.1.3. Stress distribution near gravel boundaries

The dynamic evolution process of HFs described above demonstrates that the sequential and staggered initiation of fractures are two primary modes for crossing the GB. By contrary, the sequential initiation of fractures along the GB is the dominant pattern by which the HF bypasses gravels. This section further analyzes the mechanism behind the sequential and staggered initiation modes based on the stress distribution near gravel boundaries, as shown in Fig. 12.

In the case of HFs propagating from the matrix into the gravel, the stress near the fracture tip transmits across the interface and into the gravel as the HF gradually approaches the GB (Fig. 12(a)). Because the stiffness and failure strength of gravels are higher than those of the matrix, the stress conduction from the matrix into the gravel is obstructed, which induces the HF to open the GB and to propagate along it without inducing damage fractures inside the gravel. During the HF propagation along the GB, stress accumulates at the interface gradually and spreads towards the interior of the gravel, leading to the expansion of the tensile stress concentration zone within the gravel and an increase in tensile stress. Ultimately, an IGT-HF is generated once the tensile stress inside the gravel

exceeds the tensile strength of the gravel, realizing the sequential initiation of HFs.

In the case of HFs propagating from the gravel to the matrix, the matrix initiates earlier than the interface as the HF gradually approaches the GB (Fig. 10(b) and (e)), characterized by the staggered initiation geometry. One reason is that it is easy for the stress to transmit from the gravel into the matrix, which leads to a rapid increase in tensile stress inside the matrix and the formation of a tensile stress concentration zone (Fig. 12(b)). On the other hand, the GB tends to slip because of the large angle (45.1°) between the interface and $\sigma_{\rm H}$. Although there is a shear stress concentration zone along the interface (Fig. 12(e)), the shear failure strength of the interface has not been reached, and no interface fractures have been created. Overall, it is earlier for the matrix to reach the tensile failure strength and create fractures, while the interface has a tendency to fail in shearing. In fact, a shear fracture is formed on that interface at t=16690, as shown in Fig. 10(b).

In areas B1 and B2, the HFs bypass the interfaces between two contacting gravels. In area B1, the HF diverts toward and grows along the interface between gravels G8 and G9 instead of the one between gravels G2 and G8. This behavior is probably caused by the difference in orientations of the GBs with respect to σ_H . Specifically, the orientation of the interface between gravels G8 and G9 is inclined to $\sigma_{\rm H}$ at a small angle (about 13°). However, the orientation of the interface between gravels G2 and G8 deflects away from $\sigma_{\rm H}$ at a much larger angle (up to 71°) and is opposite to the direction of HF propagation. As a result, the larger tensile deformation is generated along the interface between gravels G8 and G9, facilitating the spread of the induced stress along this interface (Fig. 12(c)). The stress transmission along the GB causes interface contacts to fail in turn during the HF bypasses gravels, realizing the sequential initiation. Moreover, a local concentration zone of shear stress is observed along the interface between gravels G8 and G9 (Fig. 12(f)), indicating that this interface is more prone to failure in shearing.

The fracture initiation mode is primarily influenced by the mechanical properties of the gravel, matrix, and interface, as well as the orientations of GBs. This study further statistically investigates the correlation between the HF-gravel interaction behavior and the

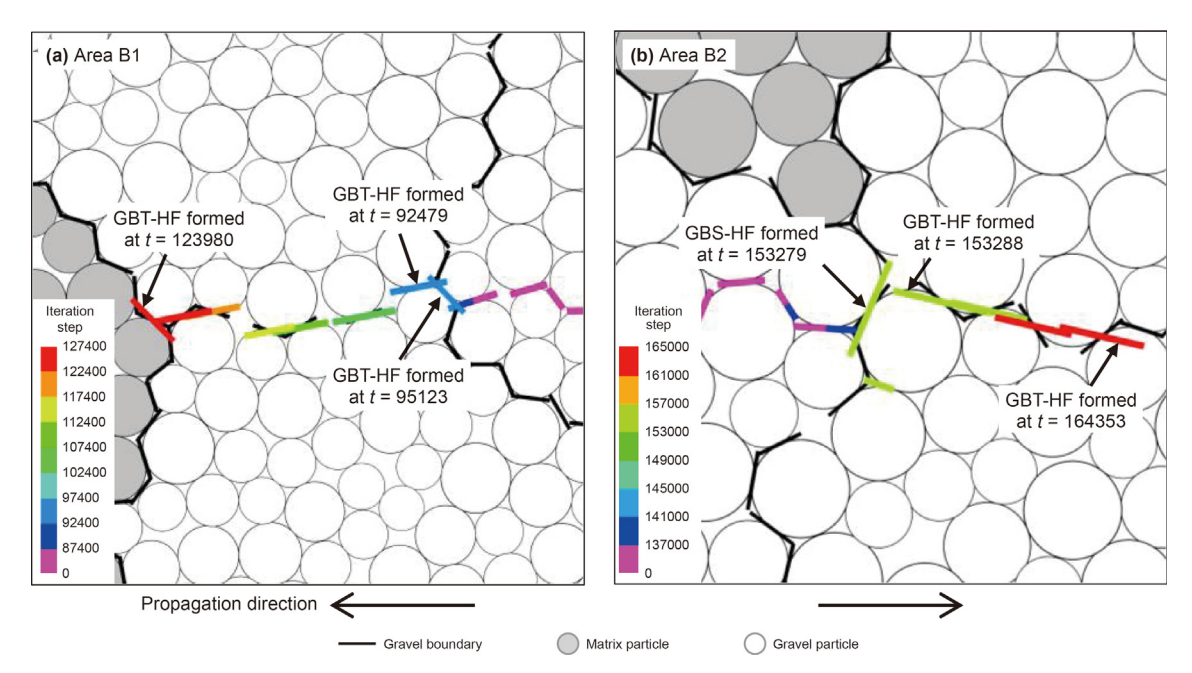


Fig. 11. The dynamic evolution process of the HF bypassing the gravel. (a) HF propagation geometry in area B1; (b) HF propagation geometry in area B2.

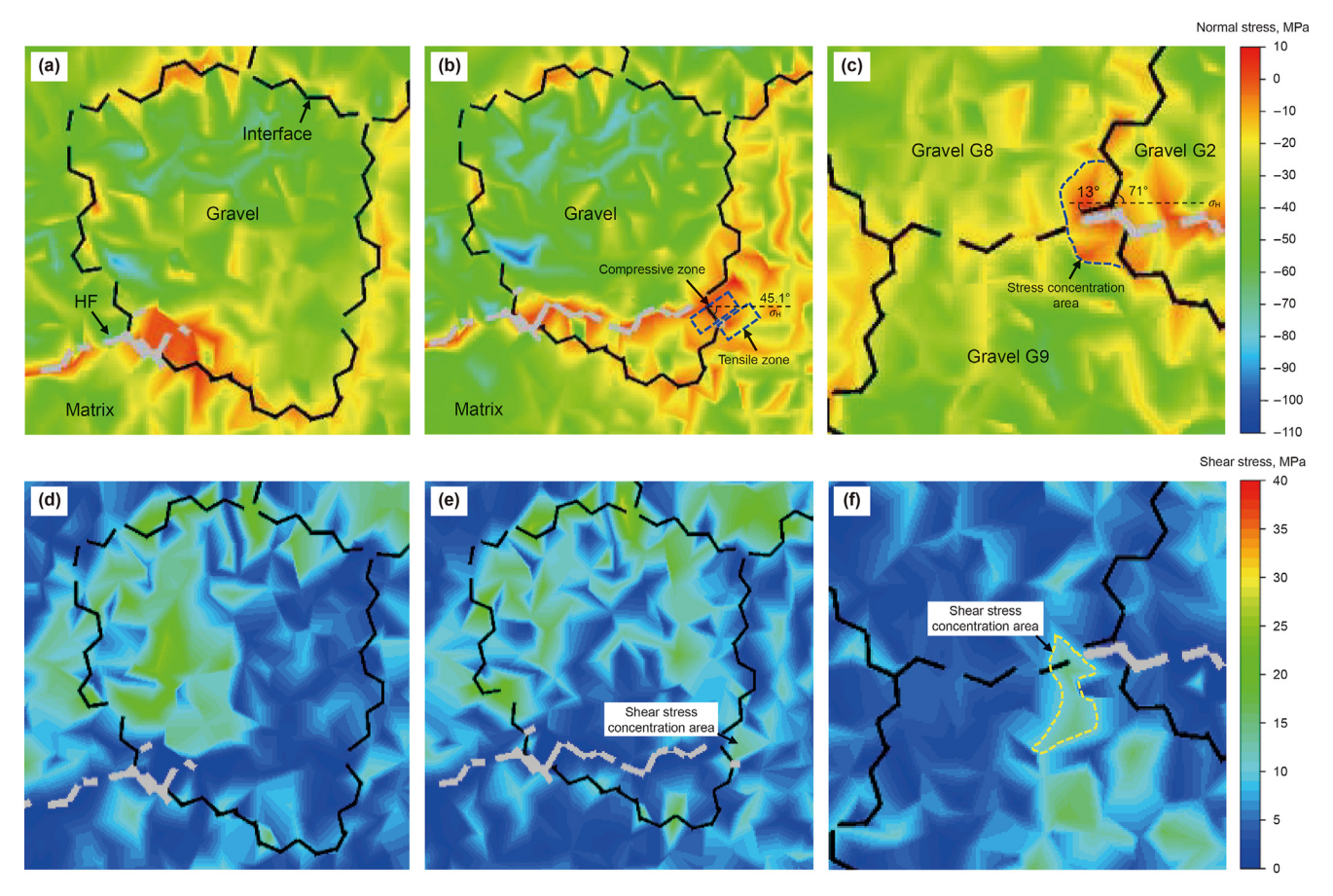


Fig. 12. The stress distribution near gravel boundaries. (**a**) and (**d**) describe the tensile and shear stresses in the case of the HF propagating from the matrix to the gravel, respectively; (**b**) and (**e**) describe the tensile and shear stresses in the case of the HF propagating from the gravel to the matrix, respectively; (**c**) and (**f**) describe the tensile and shear stresses in the case of the HF propagating along the interface between gravels, respectively.

angle of the GB with respect to σ_H . Fig. 13 reveals that the HF tends to penetrate gravels when the orientation of the GB is between 40.7° and 134.9°, i.e., the angle between the GB and σ_H is $45^\circ-90^\circ$. By contrary, the HF bypasses gravels when the orientations of the GBs are 10.9° and 167.1° , respectively, i.e., the angle between the GB and σ_H is averagely 12° . This correlation is mainly determined by the fracture energy required to maintain the fracture propagation. Bypassing a GB with a large angle will consume more fracture energy to overcome the compressive force from σ_H compared to crossing it. However, crossing a GB with a small angle will consume more fracture energy to overcome the barrier effect from the gravel

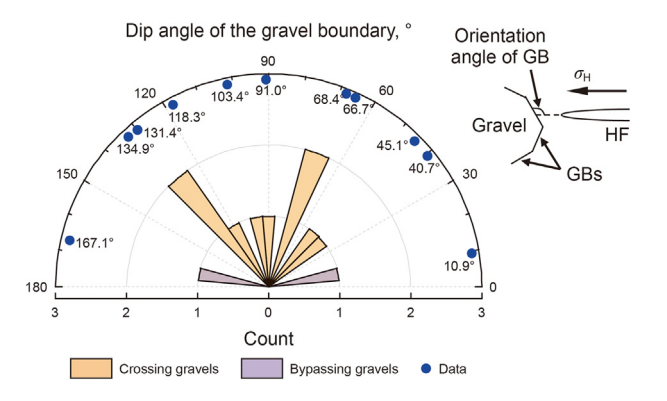


Fig. 13. The correlation between HF-gravel interaction behavior and orientations of GBs.

of high stiffness and failure strength compared to bypassing it.

3.1.4. Fracture width distribution

The width distribution of HFs is presented in Fig. 14. It is indicated that the width generally decreases from the fracture entrance to the fracture tip with fluctuations of varying amplitudes. For penetrating gravels, the HF usually deflects at the GB, leading to a significant drop in the fracture width. Specifically, the width of the left wing decreases by 48.9% and 69.8% at locations C1 and C4, respectively; the width of the right wing reduces by an average of 60.3%, with reductions of 84.4%, 54.6%, 66.2%, and 37.8% at locations C2, C3, C5, and C6, respectively. However, the fracture width tends to increase rapidly after crossing the GB due to the fracture propagation direction returning to $\sigma_{\rm H}$. For bypassing gravels in areas B1 and B2, the HF width tends to decrease monotonically along the GB.

Notably, the width decreases and fluctuates severely for the fractures inside the gravel or matrix. This is mainly attributed to different fracture types and the heterogeneity of particle sizes and mechanical properties of contacts. On the one hand, shear fractures within the gravel or matrix have much smaller widths than those of tensile fractures (e.g., the shear fracture width in the matrix on the left of the wellbore decreases by 78.8% compared to the tensile fracture created earlier). On the other hand, the contact force and contact stiffness within the gravel or matrix are highly heterogeneous, which may lead to the deflection of HFs and the increase of local tortuosity. Thus, it can be concluded that the HF width in glutenite is highly uneven. Particularly, the width decreases significantly at spots where the fracture interacts with the GB or

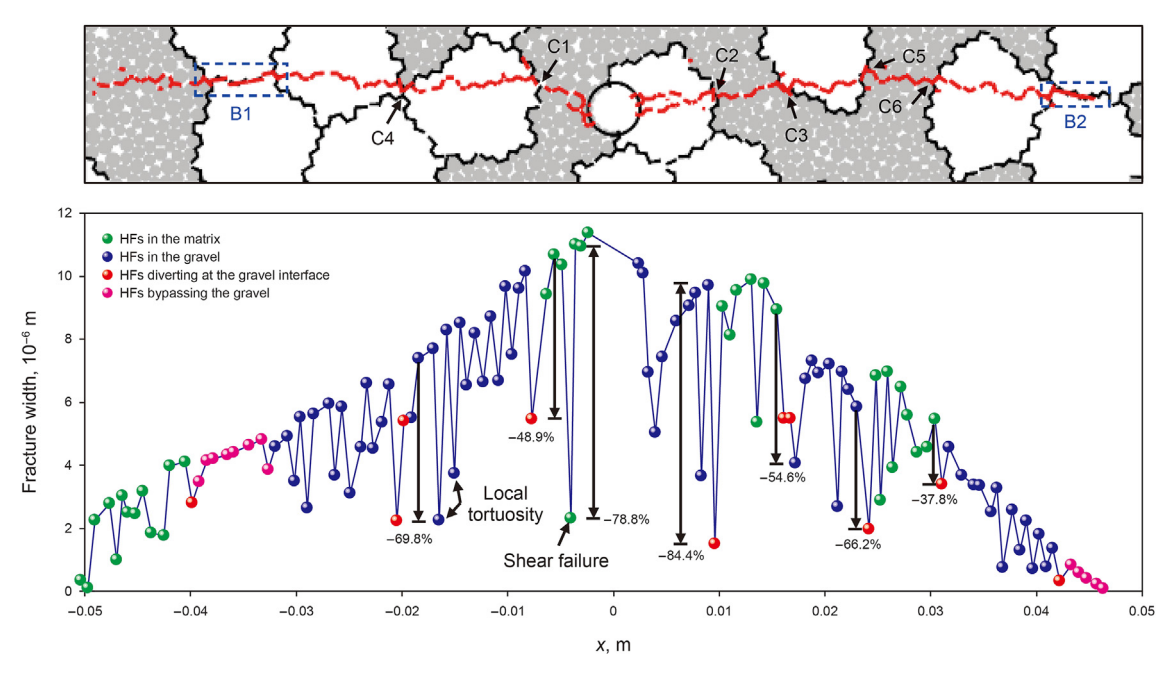


Fig. 14. The width distribution of the HF in glutenite.

deflects and bends. In hydraulic fracturing treatments, the sharp reduction of widths will increase the transport resistance of proppants, probably resulting in severe sand plug at the key positions mentioned above.

3.2. Effects of stress states on hydraulic fracture propagation in glutenite

3.2.1. Horizontal stress difference

The HF propagation geometries in glutenite under different horizontal stress differences ($\Delta \sigma$) are presented in Fig. 15. With σ_h of 30 MPa, $\Delta \sigma$ is set to 3, 6, 9, and 12 MPa, which corresponds to K_h of 0.1, 0.2, 0.3, and 0.4, respectively. Under low $\Delta \sigma$ of 3 MPa ($K_h = 0.1$), three fractures initiate at the wellbore. HF1 propagates from the matrix on the right of the wellbore and is then attracted by the nearby gravel. Afterward, HF1 propagates along the GB at a deviation angle of 34° from $\sigma_{\rm H}$. HF2 initiates at the GB and grows at a deviation angle of 30° from σ_H , penetrating two contacting gravels consecutively. HF3 also initiates at the GB but propagates in the approximate direction of σ_h . As the fracture tip moves away from the wellbore, the propagation directions of HF1 and HF2 gradually return to that of σ_H . In the case of $\Delta \sigma = 6$ MPa ($K_h = 0.2$), multiple fractures initiate at the wellbore. Differently, HF1 tends to grow in the direction of $\sigma_{\rm H}$, and the deviation angle of HF2 from $\sigma_{\rm H}$ in the near-wellbore region decreases to 19°, whereas the length of HF3 reduces significantly. When $\Delta \sigma$ increases to 9 MPa ($K_h = 0.3$), the deviation angle of HF2 from $\sigma_{\rm H}$ in the near-wellbore region further decreases to 12°, and the propagation of HF3 is suppressed, causing HF3 to be arrested within the gravel. However, under high $\Delta \sigma$ of 12 MPa ($K_h = 0.4$), a two-wing HF initiates and extends in the direction of σ_H .

It is likely that the HF propagation falls into the gravel-dominated regime under lower $\Delta\sigma$ of 3–6 MPa ($K_h=0.1$ –0.2). Hence, the complex stress distribution induced by gravels near the wellbore can lead to the initiation of multiple HFs and induce the HF to propagate at a large deviation angle from σ_H . As $\Delta\sigma$ increases, σ_H gradually dominates the fracture propagation, and the barrier

effect from the gravel is relatively undermined, promoting the HF to propagate in the direction of σ_{H} . The fracture propagation is in the stress-dominated regime under higher $\Delta\sigma$ of 9–12 MPa ($K_{\text{h}}=0.3-0.4$).

Fig. 16(a) shows that the total number of HFs reduces from 615 to 459 as $\Delta \sigma$ increases from 3 to 12 MPa. It indicates that the fracture tortuosity caused by gravels gradually decreases with the increase of $\Delta \sigma$. Fig. 16(b) indicates that tensile failure is the main mode for HF propagation in glutenite. Interestingly, among intragravel HFs (IG-HFs), the proportion of intra-gravel shear HFs (IGS-HFs) tends to increase as $\Delta \sigma$ increases, suggesting that the gravel is more susceptible to failure in shearing when the HF penetrates gravels under high $\Delta \sigma$. However, the variation of $\Delta \sigma$ has a minor impact on the shearing failure of gravel-bypassing HFs (GB-HFs).

3.2.2. Minimum horizontal stress

The effects of minimum horizontal stress (σ_h) on HF propagation geometries in glutenite are illustrated in Fig. 17. K_h is set to 0.3 in all cases. Results show that the growth of HF3 is gradually suppressed as σ_h increases, while the propagation geometries of HF1 and HF2 are similar under different minimum horizontal stresses. Fig. 18(a) suggests that the total number of HFs tends to decrease as σ_h increases from 10 to 40 MPa, indicating that the increase in σ_h somewhat reduces the local tortuosity of HFs. The tortuosity of the propagation trajectory arises from the deviation of the fracture propagation direction from σ_H . Under high σ_h of 30–40 MPa, a considerable amount of energy will be consumed to overcome the compression from σ_h if the HF propagates at a deviation angle from σ_H . Thus, the HF tends to extend straightly under high σ_h (Fig. 17(c) and (d)).

It is noteworthy in Fig. 18(b) that as σ_h increases, the proportions of IGS-HFs and GBS-HFs increase from 1.6% to 17.6% and from 4.5% to 27.8%, respectively. This phenomenon suggests that the interior and boundary of the gravel are easier to fail in shearing under high σ_h . This observation can be explained by the stress analysis in Fig. 12. Given the random arrangement of particles and the heterogeneity of contact stiffness, several local concentration zones of

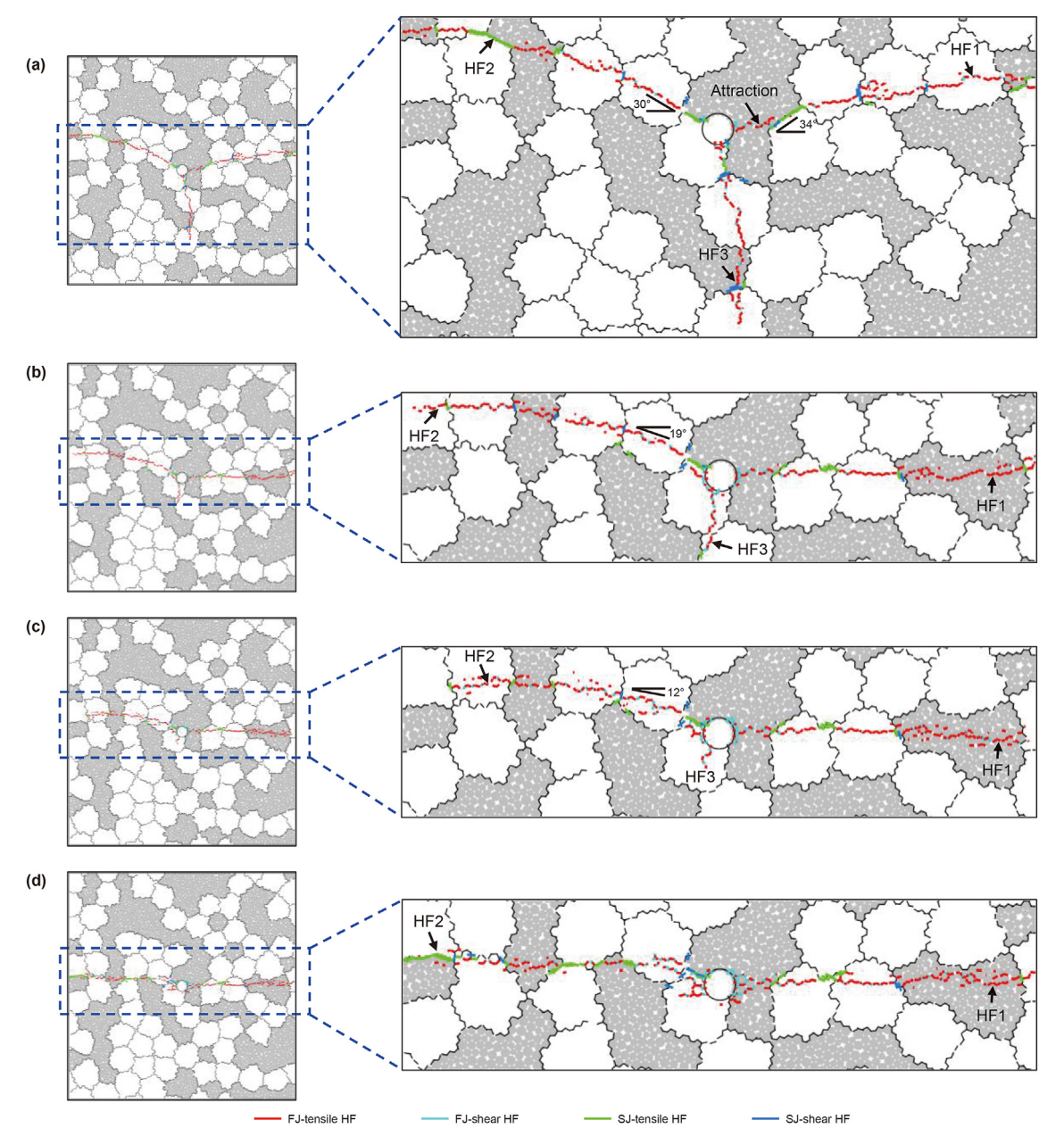


Fig. 15. The propagation geometries of HFs in glutenite under different horizontal stress differences. (a) $\Delta \sigma = 3$ MPa, $K_h = 0.1$; (b) $\Delta \sigma = 6$ MPa, $K_h = 0.2$; (c) $\Delta \sigma = 9$ MPa, $K_h = 0.3$; (d) $\Delta \sigma = 12$ MPa, $K_h = 0.4$.

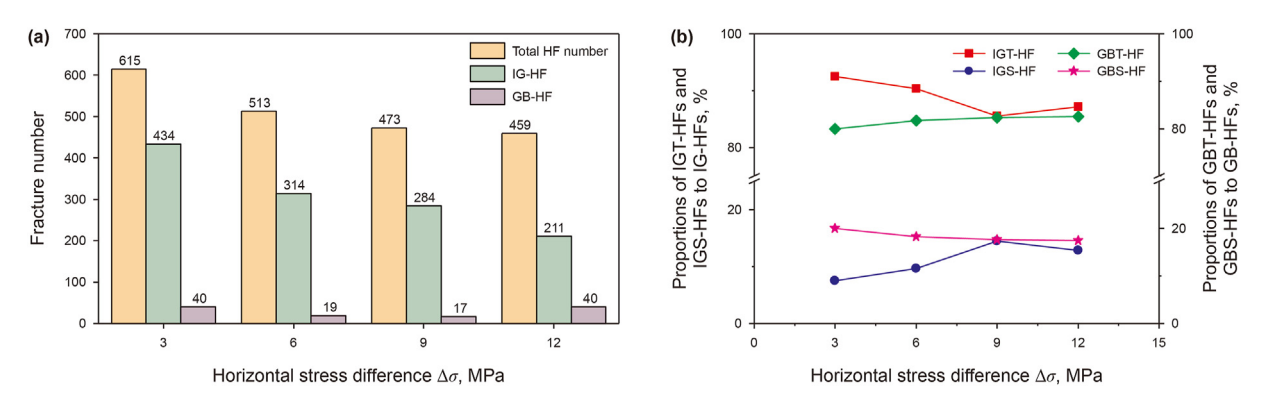


Fig. 16. The numbers and proportions of different types of HFs under varying horizontal stress differences. (a) Numbers of IG-HFs and GB-HFs; (b) Proportions of IGT-HFs, IGS-HFs, GBT-HFs, and GBS-HFs.

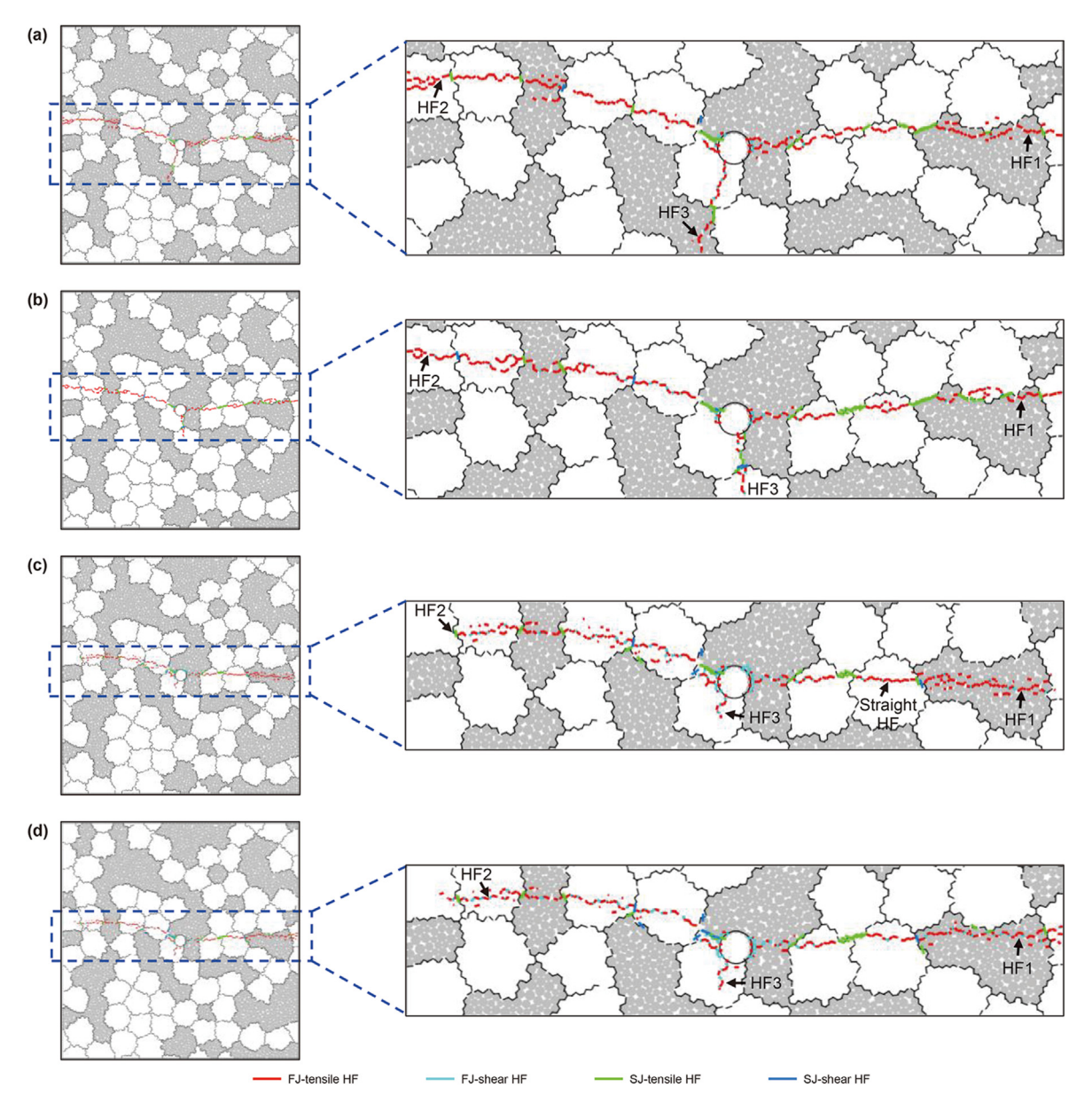


Fig. 17. The propagation geometries of HFs in glutenite under different minimum horizontal stresses. (a) $\sigma_h = 10$ MPa; (b) $\sigma_h = 20$ MPa; (c) $\sigma_h = 30$ MPa; (d) $\sigma_h = 40$ MPa.

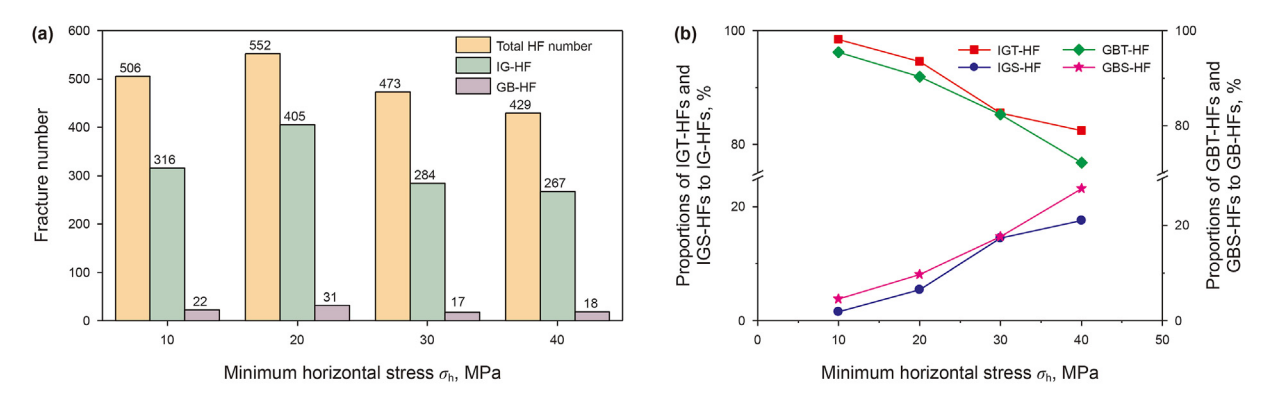


Fig. 18. The numbers and proportions of different types of HFs under varying minimum horizontal stresses. (a) Numbers of IG-HFs and GB-HFs; (b) Proportions of IGT-HFs, IGS-HFs, GBT-HFs, and GBS-HFs.

shear stress may be formed within the gravel or near the GB. Under high $\sigma_{\rm h}$, shear stresses of certain contacts in those regions approach the shear failure strength, while normal stresses of most contacts are still under compression. Consequently, the generation of shear HFs is induced more easily than tensile HFs inside gravels and at GBs.

3.3. Effects of gravel properties on hydraulic fracture propagation in glutenite

3.3.1. Gravel content

Figs. 19 and 20 illustrate the effects of gravel contents (V_g) on the HF propagation geometries and numbers and proportions of different types of HFs, respectively. It is found that under high V_g , the HFs can extend approximately along the direction of σ_H (Fig. 19(d)), and the number of IG-HFs is significantly more than that of GB-HFs (Fig. 20(a)). This suggests that densely-distributed gravels seem not to have a strong hindering effect on HF

propagation. Actually, stress still predominates in HF propagation in glutenite with high $V_{\rm g}$, making penetrating gravels the primary interaction behavior. According to Fig. 20(a), the total numbers of HFs are 466 and 473 when gravel contents are 50% and 60%, respectively. However, the total numbers increase to 586 and 503 when gravel contents reach 70% and 80%, respectively. This indicates that the fracture tortuosity is enhanced with the increase of $V_{\rm g}$ due to complex interaction behavior between HFs and gravels. Furthermore, as the HF crosses the GB, several meso-scale complex fracture geometries, such as stepping growth (i.e., deflection toward the GB), bifurcation, and fracture clusters, may be formed, as shown in Fig. 19. The higher the gravel content is, the more frequently the fracture tip interacts with GBs, consequently resulting in more complex fracture geometries locally and increasing the fracture tortuosity.

The number of GB-HFs tends to rise with the increasing $V_{\rm g}$. GB-HFs are comprised of fractures propagating continuously along the interface between gravels or between the gravel and matrix as well

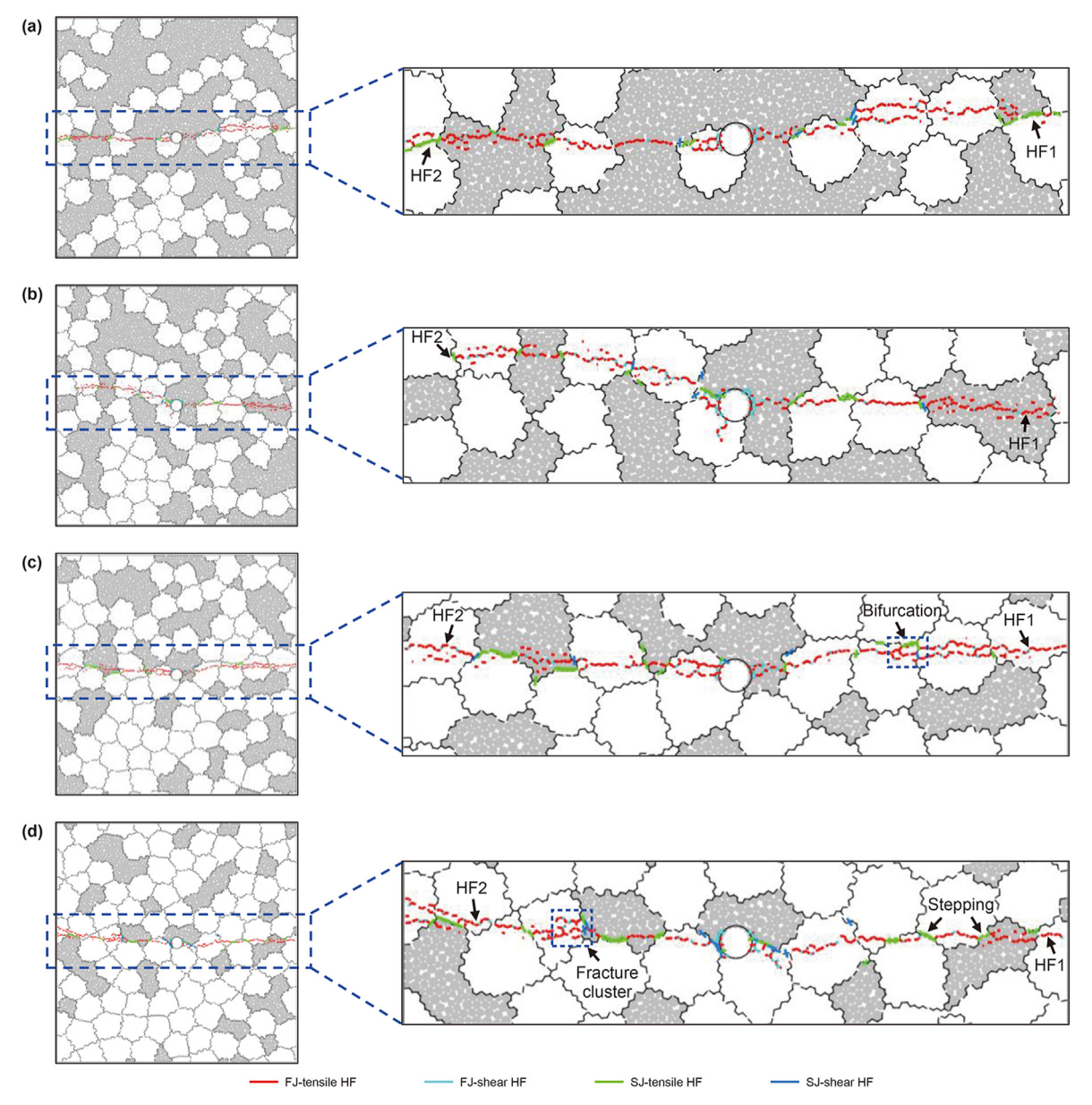
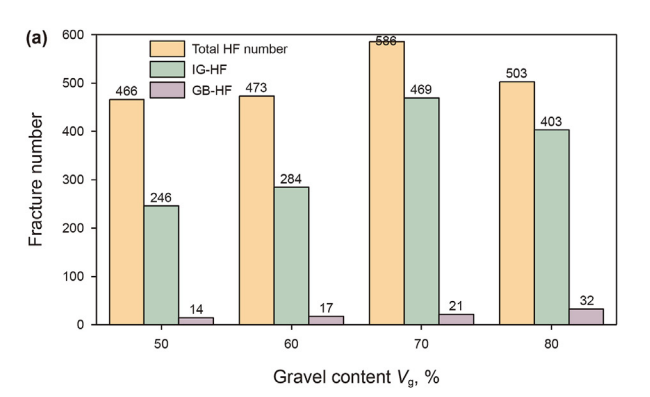


Fig. 19. The propagation geometries of HFs in glutenite under varying gravel contents. (a) $V_g = 50\%$; (b) $V_g = 60\%$; (c) $V_g = 70\%$; (d) $V_g = 80\%$.



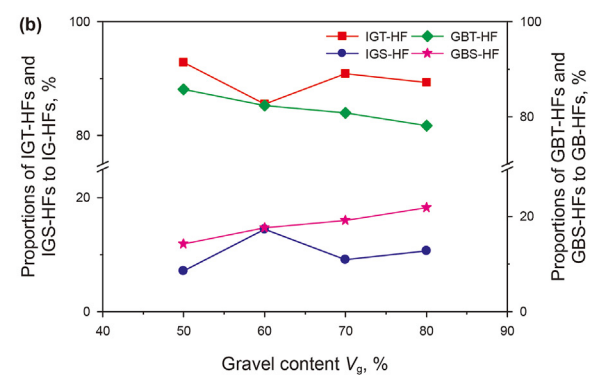


Fig. 20. The numbers and proportions of different types of HFs under varying gravel contents. (a) Numbers of IG-HFs and GB-HFs; (b) Proportions of IGT-HFs, IGS-HFs, GBT-HFs, and GBS-HFs

as those deflecting toward GBs while penetrating gravels. A lower gravel content (e.g., $V_{\rm g}=50\%-60\%$) results in a reduction in the interaction frequency between the fracture tip and gravels, thus few GB-HFs are created. Conversely, a higher gravel content (e.g., $V_{\rm g}=70\%-80\%$) leads to more frequent HF-gravel interactions, with the number of GB-HFs increasing. In addition, the proportions of IGS-HFs and GBS-HFs tend to rise as $V_{\rm g}$ increases (Fig. 20(b)). The high gravel content enhances the compression within gravels and slippage at GBs, leading to an increase in the number of shear stress concentration zones. Therefore, a greater number of shear HFs may

be generated during fracturing the glutenite with higher gravel contents.

3.3.2. Gravel size

HF propagation geometries under varying gravel sizes $(d_{\rm g})$ are presented in Fig. 21. It is observed that the barrier effect of gravels on HF growth is enhanced with the increase of $d_{\rm g}$, correspondingly enlarging the deviation angle of HF propagation from $\sigma_{\rm H}$. In finegrained glutenite $(d_{\rm g}=4-6~{\rm mm})$, gravels densely distribute around the wellbore, forming a complex stress field in the near-

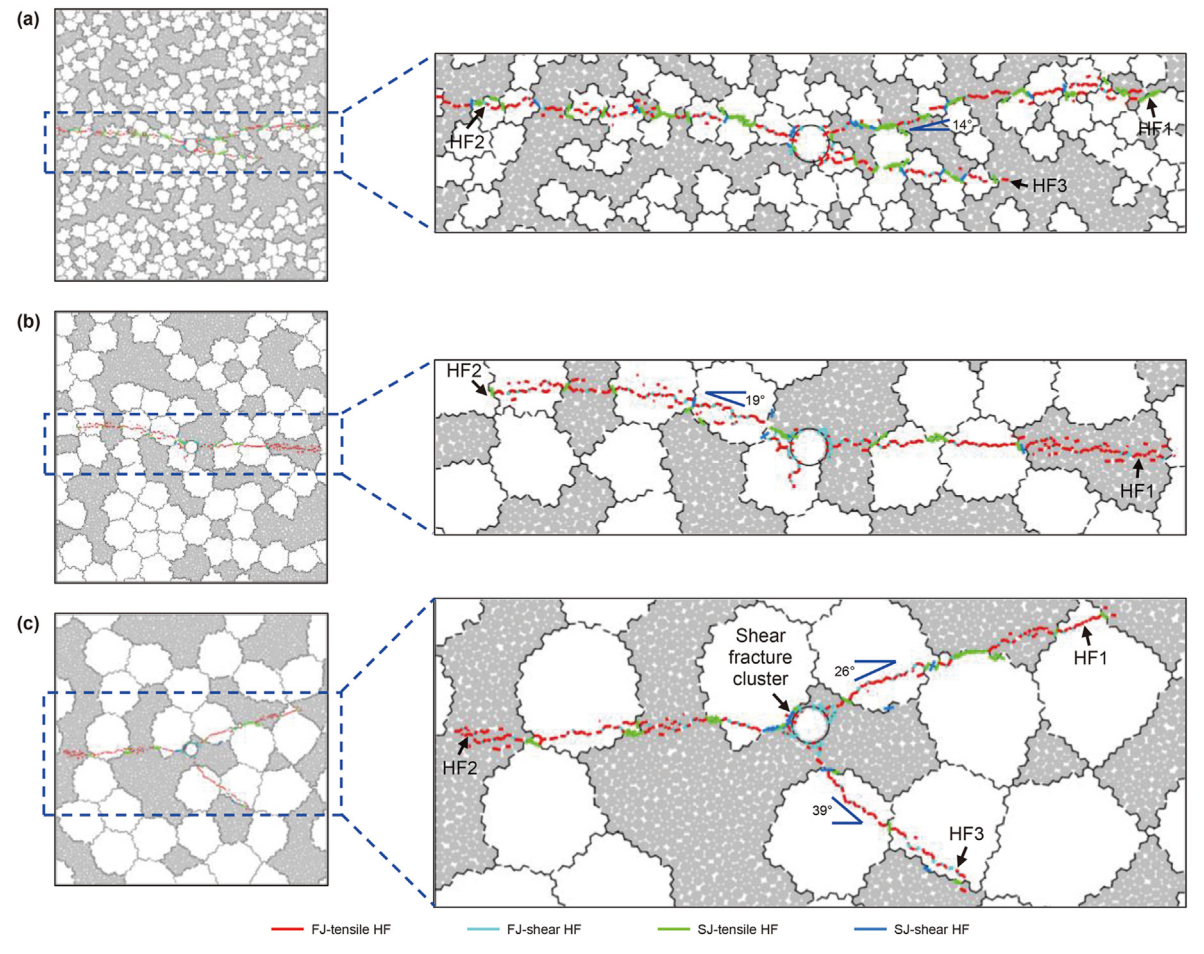


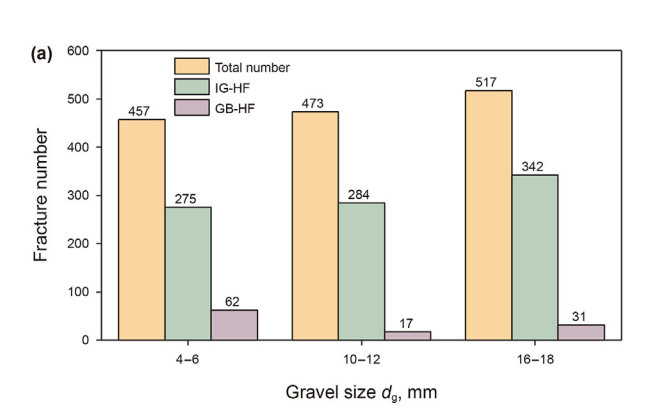
Fig. 21. The propagation geometries of HFs in glutenite under different gravel sizes. (a) $d_g = 4-6$ mm; (b) $d_g = 10-12$ mm; (c) $d_g = 16-18$ mm.

wellbore region during fracturing, thereby initiating multiple HFs. However, the barrier effect of small gravels is weaker than medium-sized and large gravels. Although the HFs in fine-grained glutenite bypass gravels frequently (the number of GB-HFs reaches 62), HF2 and HF3 can still extend approximately along the direction of $\sigma_{\rm H}$, with HF1 deviating at a small angle of 14°, as shown in Fig. 21(a). In coarse-grained glutenite ($d_g = 14-16$ mm), large gravels of high stiffness and strength tend to create a strong barrier effect on HF propagation. The large gravels near the wellbore make it difficult for the HF to initiate, thereby leading to the generation of damage fracture clusters at GBs during pressure accumulation. Ultimately, multiple HFs initiate from the wellbore (Fig. 21(c)). Additionally, the number of GB-HFs in coarse-grained glutenite is less than that in fine-grained glutenite (Fig. 22(a)). This suggests that the HFs in coarse-grained glutenite tend to penetrate gravels. Nevertheless, the fracture propagation direction within large gravels may deflect from $\sigma_{\rm H}$ significantly. It can be seen that HF1 and HF3 extend inside gravels at deviation angles of about 26° and 39°, respectively.

Further analysis in combination with Fig. 22(b) shows that the proportion of IGS-HFs in fine-grained glutenite are less than that in glutenite with medium-sized and large gravels. The reason behind this finding is that the HF propagates within large gravels at a large deviation angle from $\sigma_{\rm H}$, which makes it easier to induce shear failure. Moreover, the proportion of IGS-HFs in fine-grained glutenite are higher than that in coarse-grained glutenite. In general, it is easy for the stress to transmit across small gravels. Thus, the shear stress is prone to concentrate near GBs in fine-grained glutenite under stress superposition, leading to the wide distribution of GBS-HFs. On the contrary, the stress transmission in coarse-grained glutenite is significantly hindered by large gravels, causing most of the GBS-HFs to gather in the near-wellbore region.

3.3.3. Stiffness ratio of the gravel to matrix

Fig. 23 exhibits the HF propagation geometries in glutenite with varying stiffness ratios of the gravel to matrix ($R_{\rm S}$). Usually, the stiffness ratio of the argillaceous glutenite is larger than that of the sandy glutenite. It is observed that the offset along the GB lengthens while penetrating gravels, as $R_{\rm S}$ increases from 2 to 4. This leads to an increase in the number of GB-HFs from 17 to 28 (Fig. 24(a)). In the case of $R_{\rm S}=4$ (sandy glutenite), the significant difference in stiffness between the gravel and matrix makes it challenging for the stress near the fracture tip to transmit across the GB into the gravel. Compared to sandy glutenite with small $R_{\rm S}$, more energy accumulates at GBs before the HF penetrates gravels in argillaceous glutenite with large $R_{\rm S}$, hence leading to larger deformation at GBs and the creation of more GB-HFs.



As R_s increases, the deviation angle of fracture propagation within gravels and fracture tortuosity tend to increase. For instance, given $R_s = 2$, the propagation direction of HF1 is inclined to σ_H , and the deviation angle of HF2 is about 12°. With R_s growing to 3, HF1 propagates at a deviation angle of 10° in the near-wellbore region, and HF2 penetrates gravels successively at a deviation angle of 28°. with the total HF number increasing to 359. When R_s reaches 4, the deviation angle of HF1 near the wellbore increases to 16°, and the deviation angle of HF2 is close to 29°, with the total HF number further increasing to 409. This phenomenon suggests that the stress transmission varies under different stiffness ratios, thus forming different stress distributions within gravels. Fig. 24(b) further indicates that the proportion of IGS-HFs tends to increase slightly as R_s increases, but that of GBS-HFs increases significantly, with some GBT-HFs transforming to GBS-HFs. This is because the high R_s creates a huge difference in deformation between the gravel and matrix, which enhances the tendency to slip along GBs.

4. Discussion

This paper focuses on the interaction behavior between HFs and gravels in glutenite. This study utilized Voronoi tessellation to generate gravels distributing randomly, successfully representing the inherent contact characteristics between gravels. Additionally, a grain-based hydro-mechanical coupling model for hydraulic fracturing in glutenite was established using the pore network. The key findings are that the primary interaction behavior between HFs and gravels in glutenite is penetrating the gravel; with the increase of $\Delta\sigma$, $\sigma_{\rm h}$, $V_{\rm g}$, $d_{\rm g}$, and $R_{\rm s}$, more IGS-HFs are formed during fracturing the glutenite.

4.1. Dominant HF-gravel interaction behavior

Some experts have carried out fracturing experiments in glutenite (Liu et al., 2016; Yu et al., 2021; Ma et al., 2017) and believed that HFs tend to bypass gravels when encountering them due to the higher strength of the gravel compared to the matrix, which creates a barrier effect on HF propagation. However, other experts argued that HFs can penetrate gravels if the stress predominance on HF propagation is enhanced (i.e., $\Delta\sigma$ increases) or the barrier effect of gravels is undermined (i.e., d_g reduces) (Zou et al., 2021; Shi et al., 2023; Liu et al., 2019). Simulation results in this study show that the HF can penetrate gravels under low $\Delta\sigma$ or in coarse-grained glutenites, and the proportion of IG-HFs exceeds 80%, while the proportion of GB-HFs ranges from 4.3% to 18.4%.

The discrepancy between experimental and numerical results in this study may be attributed to the damaged GBs generated during

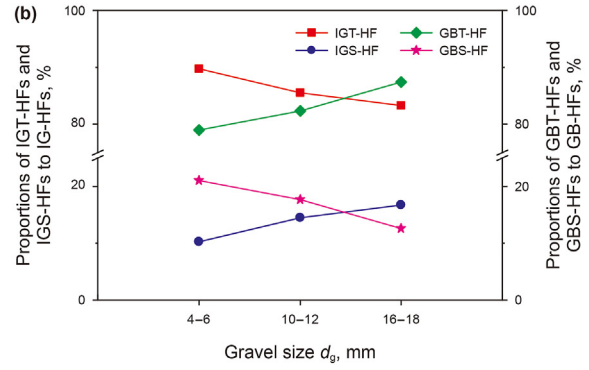


Fig. 22. The numbers and proportions of different types of HFs under varying gravel sizes. (a) Numbers of IG-HFs and GB-HFs; (b) Proportions of IGT-HFs, IGS-HFs, GBT-HFs, and GBS-HFs.

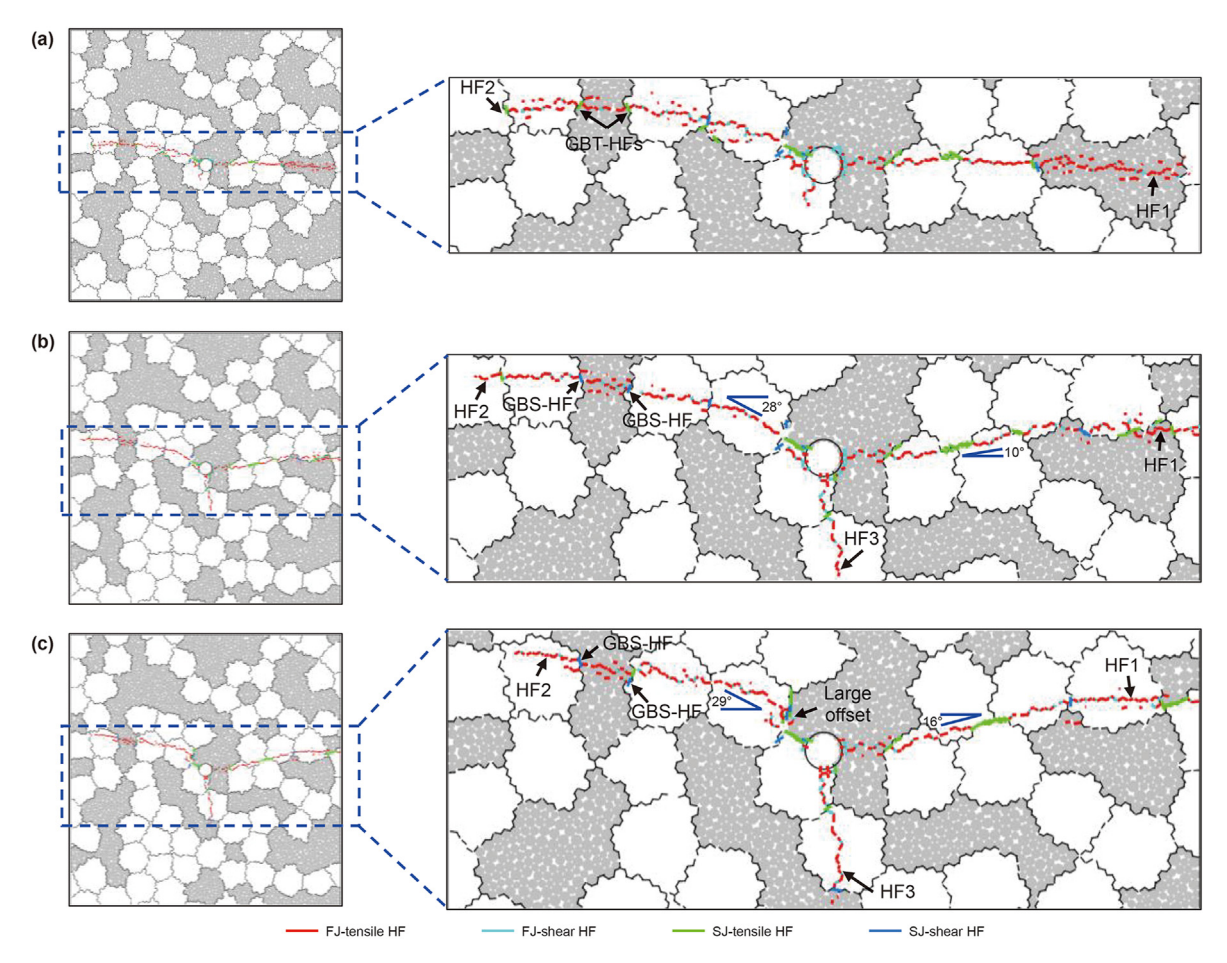


Fig. 23. The propagation geometries of HFs in glutenite under varying stiffness ratios. (a) $R_s = 2$; (b) $R_s = 3$; (c) $R_s = 4$.

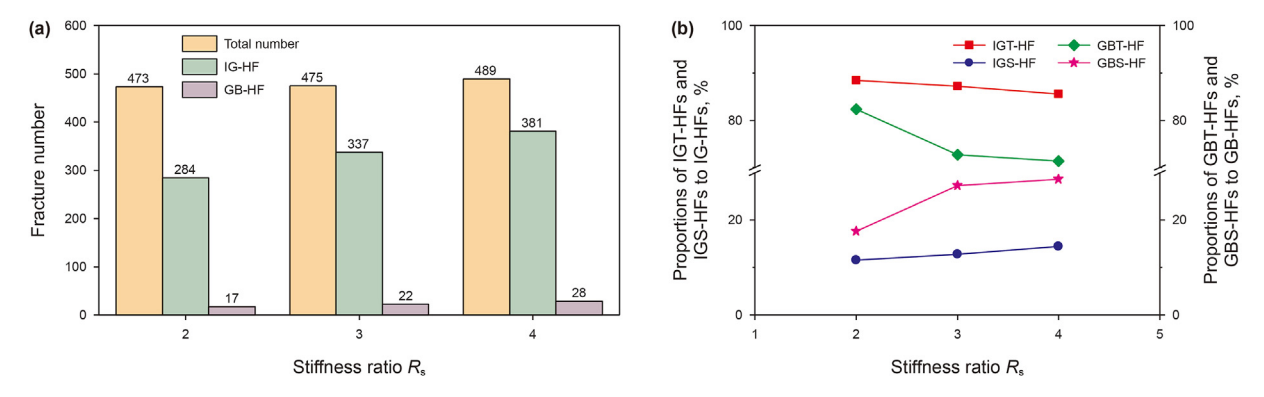


Fig. 24. The numbers and proportions of different types of HFs under varying stiffness ratios. (a) Numbers of IG-HFs and GB-HFs; (b) Proportions of IGT-HFs, IGS-HFs, GBT-HFs, and GBS-HFs.

fracturing experiments. The glutenite cores used in some experiments may have strong water sensitivity, and cementation of gravels is poor. This can induce the generation of damage fractures at GBs, even leading to the detachment of gravels, if clean water is utilized to process the cores (Zhang et al., 2022). When the HF meets the damaged GBs, the pre-existing interface fractures will induce the HF to propagate along the GBs. Additionally, inconsistency in the loading rates of tri-axial stresses may also lead to the generation of damage fractures at GBs because of the shear stress concentration within specimens. Basically, the magnitude of stress applied in laboratories is lower than that in reservoirs, making it

hard to compact those damage fractures well. For numerical simulations, there is no such issues as damaged GBs to be considered.

This study suggests that GB-HFs can be formed when orientations of GBs that HFs intersect with are inclined to $\sigma_{\rm H}$. Besides, a short GB-HF deflecting along the GB may be created while penetrating gravels, forming the stepping propagation geometry. Ma et al. (2017) observed the similar HF growth geometries in experiments and believed that the HF prefers a trajectory of the least propagation resistance. In other words, the magnitude of the propagation resistance determines the interaction behavior between HFs and gravels. For instance, if an HF bypasses the gravel at

a large deviation angle from σ_H , it must overcome the compression from σ_H , making the propagation resistance in bypassing the gravel larger than that in penetrating the gravel. In this case, the HF tends to penetrate the gravel.

This paper demonstrates that penetrating the gravel is the dominant interaction behavior between HFs and gravels. Penetrating the gravel follows the sequential and staggered initiation mode. In fact, some scholars have verified the possibility of HFs penetrating gravels. Shi et al. (2023) pointed out in their experiments that HFs tend to penetrate gravels in the near-wellbore region. The numerical simulations by Huang et al. (2023) and Yu et al. (2023) also indicated that there are a large number of gravel-penetration fractures generated during fracturing glutenite.

4.2. Shear failure of gravels and interfaces

This paper presents the proportions of shear fractures under different horizontal stress differences, minimum horizontal stresses, gravel contents, gravel sizes, and stiffness ratios of the gravel to matrix. It is indicated that IGS-HFs tend to be generated in coarse-grained glutenite under high $\Delta\sigma$, whereas GBS-HFs tend to be created in argillaceous glutenite with large $R_{\rm S}$. Moreover, the proportions of IGS-HFs and GBS-HFs increase as $\sigma_{\rm h}$ and $V_{\rm g}$ increase.

Relevant studies of the types of HFs in glutenite were rarely reported. Some experts applied the acoustic emission monitoring technology to preliminarily determine the HF types in glutenite in laboratories. The localization results of acoustic events by Liu et al. (2019) show that the proportion of shear fractures ranges from 33.3% to 61.8%, and this proportion increases with the increasing gravel size. The proportion of shear fractures in this study is less than 20%.

The discrepancy in the proportion of shear fractures can be attributed to two main reasons. Firstly, the way microscopic contact parameters are calibrated in DEM models plays a significant role. Previous studies usually calibrated those parameters based on experimental stress-strain curves (Potyondy and Cundall, 2004; Hsieh et al., 2008; Hofmann et al., 2015; Peng et al., 2018; Zhou et al., 2019). By adjusting the values of contact parameters, the stress-strain curve in DEM simulations can match that in mechanical tests, hence approximating the macroscopic mechanical behavior of rocks. Since there are multiple suitable combinations of microscopic parameter values, using the stress-strain curve as the main calibration criterion may not necessarily match the experimental results in terms of proportions of tensile and shear fractures. To address this, it is important to conduct acoustic emission monitoring during mechanical tests and take interpretation results of the number and location of tensile and shear fractures as the calibration criterion.

Secondly, the difference in identification mechanisms of shear fractures between experimental monitoring and DEM model may lead to this discrepancy. The acoustic emission monitoring in experiments identifies tensile and shear fractures based on relative displacements of fracture surfaces calculated by moment tensor inversion. Typically, a shear fracture is identified when the normal strain of fracture surfaces is less than the shear strain. However, DEM differentiates tensile and shear fractures by the strength envelope. A shear fracture is identified when the shear stress on the contact meets the shear strength, and the tensile stress is less than the tensile strength. To align with the proportion of shear fractures in experiments, Kong et al. (2022) combined these two identification mechanisms and proposed a novel calibration criterion based

on the critical internal friction angle.

It is noted that there has historically been a mismatch regarding the amount of shearing between the DEM simulation and laboratory observation in hydraulic fracturing, and the results of numerical simulations are not necessarily incorrect despite this discrepancy. Although the proportion of shear fractures in this paper is lower than that in laboratory observations, the variation laws of the proportion of shear fractures under different influencing factors remain affected. For example, it has been observed that the proportion of shear fractures increases with increasing d_g , which is consistent with previous experimental results (Zou et al., 2021; Ma et al., 2017).

In glutenite, the uneven distribution of mechanical properties will disturb the propagation directions of HFs within gravels, causing the orientations of IG-HFs to deviate from $\sigma_{\rm H}$ and forming shear fractures. The level of disturbance to the propagation direction of IG-HFs varies under different stress states, gravel properties, and stiffness ratios, creating different deviation angles for the orientations of IG-HFs and, thus, affecting the proportion of shear fractures formed during fracturing. Wu et al. (2022a, 2022b) state that shear fractures tend be generated during the HFs interact with discontinuities such as bedding planes, natural fractures, and gravel interfaces. This is because the stress distribution is complex near these discontinuities. This study suggests that the number of shear stress concentration zones within gravels or at interfaces tends to increase as $\sigma_{\rm h}$ and $V_{\rm g}$ increase, which facilitates the generation of shear fractures.

Therefore, it can be inferred that the number of shear fractures formed during fracturing is likely to be considerable in real glutenite reservoirs. Particularly, a large number of shear fractures may be created while penetrating gravels. This speculation can be confirmed through underground coring tests.

4.3. Field implication

Take the glutenite oil reservoirs in Mahu Sag of Junggar Basin as an example. σ_h and σ_H in Mahu glutenite oil reservoirs are 40.9–78.6 MPa and 53.1–116.8 MPa, respectively, with $\Delta\sigma$ ranging from 12.2 to 18.2 MPa and K_h ranging from 0.21 to 0.35 (Li et al., 2020). V_g in this reservoir is 54%–78%, and d_g spans widely, varying from 2 to 64 mm (Zang et al., 2022). Lithofacies vary frequently, mainly including sandy glutenite with small R_s and argillaceous glutenite with large R_s .

A novel propagation pattern for HFs in Mahu glutenite oil reservoirs is proposed by combining the numerical results in this paper with the reservoir conditions (Fig. 25). Overall, stress dominates the direction of fracture propagation due to the high $\Delta\sigma$ or $K_{\rm h}$, and penetrating the gravel is the primary interaction behavior between HFs and gravels. In addition, an offset will be formed along the GB while penetrating the gravel, indicating a stepping propagation geometry; the larger $R_{\rm S}$ is, the longer the offset is. The HF tends to deviate from $\sigma_{\rm H}$ within the gravel, and bifurcation may occur in coarse-grained glutenite. Furthermore, the proportion of shear fractures increases with the increase of $V_{\rm g}$ and $d_{\rm g}$.

This study mainly investigated how geological properties affect the HF-gravel interaction behavior. Other key factors may dominate the HF propagation geometries in glutenite formations, e.g., perforation arrangement strategies. However, due to several limitations, this study is unable to thoroughly investigate the influences of these factors. Firstly, the model used in this study is a 2D one. However, HFs interact with gravels in the 3D space, resulting in

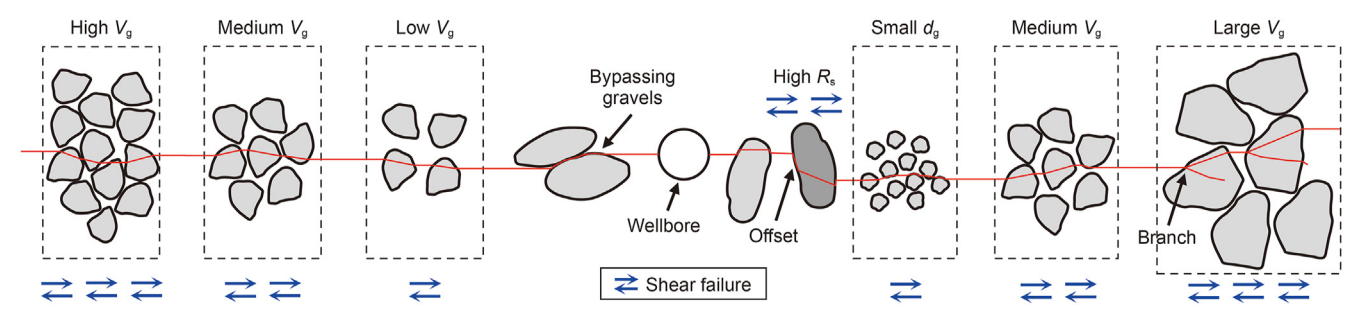


Fig. 25. The novel HF propagation pattern of glutenite oil reservoirs in Mahu Sag of Junggar Basin. The double-arrow symbol represents the shear failure of gravels and interfaces. The more symbols there are, the larger the proportion of shear fractures are.

complex fracture geometries (e.g., twisted HFs) and strong heterogeneity of fracture width in the direction of fracture height. Thus, it is necessary to develop a 3D hydraulic fracture propagation model in glutenite. Secondly, the gravel is represented as a 2D polygon. Although this allows for the rapid generation of many random gravels with different gravel sizes and contents and the characterization of area-contacting behavior between gravels, there is still a gap in geometry and distribution characteristics between the 2D numerical and real gravels. Hence, a 3D gravel generation algorithm is supposed to be developed by combining the digital core and image processing methods (Ghazvinian et al., 2014). Thirdly, the computational efficiency of this model needs improvement. The current model relies on an explicit iterative algorithm for the hydro-mechanical coupling, which, to a large extent, depends on the high-performance hardware. The limited computational capacity prevents the establishment of large-scale models at the order of magnitude of millions of particles. In the future, a fracture propagation DEM model based on GPU computation (Lisjak et al., 2018) should be developed to enhance the simulation efficiency and increase the model scale.

5. Conclusions

A grain-based HF propagation model for glutenite was established based on the particle discrete element method in this paper. Using this model, this study investigated the dynamic evolution characteristics of HFs in glutenite and analyzed the effects of various geological factors such as horizontal stress difference, minimum horizontal stress, gravel content, gravel size, and stiffness ratio of gravel to matrix on HF propagation geometries in glutenite. The main conclusions are as follows.

- (1) HFs in glutenite tend to initiate asynchronously. Penetrating the gravel is the primary HF-gravel interaction behavior. When the orientation of the GB deviates from σ_H at a large angle, the HF is prone to penetrate the gravel after interacting with that GB. An offset is usually formed along the GB while penetrating gravels, indicating a stepping propagation geometry. Penetration from the matrix into gravel follows the sequential initiation mode, while growth from the gravel into matrix obeys the staggered initiation mode. Bypassing the gravel is the secondary HF-gravel interaction behavior. When the orientation of the GB is inclined to σ_H , the HF tends to bypass the gravel after meeting that GB, with the gravel-bypassing behavior following the sequential initiation mode.
- (2) The fracture width decreases with fluctuation from the fracture entrance to the tip, and the widths of IG-HFs fluctuate more violently than GB-HFs. The offset along the GB will lead to a decrease rate of 37.8%—84.4% in fracture width.

- Moreover, the widths of shear fractures can be 78.8% less than those of tensile fractures.
- (3) Stress dominates the direction of fracture propagation. Nevertheless, the HFs may deviate from $\sigma_{\rm H}$ within gravels. The deviation angle inside gravels decreases with the increase of $\Delta\sigma$ and increases with the increase of $d_{\rm g}$ and $R_{\rm s}$. In coarse-grained glutenite with $V_{\rm g}=70\%-80\%$, the deviation angle can exceed 20° , with branches formed. In argillaceous glutenite with $V_{\rm g}=70\%-80\%$, the deviation angle can reach 30° , and the offset may increase.
- (4) IGS-HFs tend to be generated in coarse-grained glutenite under high $\Delta\sigma$. More GBS-HFs tend to be created in argillaceous glutenite with higher $R_{\rm S}$ than in sandy glutenite with lower $R_{\rm S}$. Additionally, the proportions of IGS-HFs and GBS-HFs will increase as $\sigma_{\rm h}$ and $V_{\rm g}$ increase.

Data availability

The data that has been used is confidential.

CRediT authorship contribution statement

Zhao-Peng Zhang: Writing — original draft, Visualization, Validation, Methodology, Investigation, Funding acquisition, Conceptualization. **Yu-Shi Zou:** Formal analysis, Data curation. **Hai-Yan Zhu:** Writing — review & editing, Software. **Shi-Cheng Zhang:** Supervision, Project administration.

Declaration of competing interest

The authors declare that they have no known competing financial interests or personal relationships that could have appeared to influence the work reported in this paper.

Acknowledgments

This work was supported by the National Natural Science Foundation of China (Grant No. 52304003), the Natural Science Foundation of Sichuan Province (Grant No. 2024NSFSC0961), and the Postdoctoral Fellowship Program of CPSF (Grant No. GZB20230090).

References

Al-Busaidi, A., Hazzard, J.F., Young, R.P., 2005. Distinct element modeling of hydraulically fractured Lac du Bonnet granite. J. Geophys. Res. Solid Earth 110, B06302. https://doi.org/10.1029/2004JB003297.

Beugelsdijk, L.J., de Pater, C.J., Sato, K., 2000. Experimental hydraulic fracture propagation in a multi-fractured medium. In: SPE Asia Pacific Conference on

Integrated Modelling for Asset Management. https://doi.org/10.2118/59419-MS. Chen, Y., Nagaya, Y., Ishida, T., 2015. Observations of fractures induced by hydraulic fracturing in anisotropic granite. Rock Mech. Rock Eng. 48 (4), 1455–1461. https://doi.org/10.1007/s00603-015-0727-9.

- Fabjan, T., Ivars, D.M., Vukadin, V., 2015. Numerical simulation of intact rock behavior via continuum and Voronoi tessellation models - a sensitivity analysis. Acta Geotech. Slov. 12 (2), 4–23.
- Ghazvinian, E., Diederichs, M.S., Quey, R., 2014. 3D random Voronoi grain-based models for simulation of brittle rockdamage and fabric-guided micro-fracturing. J. Rock Mech. Geotech. 6, 506–521. https://doi.org/10.1016/j.jrmge.2014.09.001.
- Hofmann, H., Babadagli, T., Yoon, J.S., Zang, A., Zimmermann, G., 2015. A grain based modeling study of mineralogical factors affecting strength, elastic behavior and micro fracture development during compression tests in granites. Eng. Fract. Mech. 147, 261–275. https://doi.org/10.1016/j.engfracmech.2015.09.008.
- Hsieh, Y., Li, H., Huang, T., Jeng, F., 2008. Interpretations on how the macroscopic mechanical behavior of sandstone affected by microscopic properties—revealed by bonded-particle model. Eng. Geol. 99, 1–10. https://doi.org/10.1016/ j.enggeo.2008.01.017.
- Huang, L., Liu, J., Zhang, F., Dontsov, E., Damjanac, B., 2019. Exploring the influence of rock inherent heterogeneity and grain size on hydraulic fracturing using discrete element modeling. Int. J. Solid Struct. 176–177, 207–220. https:// doi.org/10.1016/j.ijsolstr.2019.06.018.
- Huang, L., He, R., Yang, Z., Tan, P., Chen, W., Li, X., Cao, A., 2023. Exploring hydraulic fracture behavior in glutenite formation with strong heterogeneity and variable lithology based on DEM simulation. Eng. Fract. Mech. 278, 109020. https://doi.org/10.1016/j.engfracmech.2022.109020.
- Isaka, B.L.A., Ranjith, P.G., Rathnaweera, T.D., Perera, M.S.A., Kumari, W.G.P., 2019. Influence of long-term operation of supercritical carbon dioxide based enhanced geothermal system on mineralogical and microstructurally-induced mechanical alteration of surrounding rock mass. Renew. Energy 136, 428–441. https://doi.org/10.1016/j.renene.2018.12.104.
- Ivars, D.M., Potyondy, D.O., Pierce, M., Cundall, P.A., 2008. The smooth-joint contact model. In: 5th European Congress on Computational Methods in Applied Sciences and Engineering.
- Kong, L., Ranjith, P.G., Li, B.Q., 2021. Fluid-driven micro-cracking behaviour of crystalline rock using a coupled hydro-grain-based discrete element method. Int. J. Rock Mech. Min. Sci. 144, 104766. https://doi.org/10.1016/ j.ijrmms.2021.104766.
- Kong, L., Ranjith, P.G., Li, B.Q., Song, Y., 2022. Rock grain-scale mechanical properties influencing hydraulic fracturing using Hydro-GBM approach. Eng. Fract. Mech. 262, 108227. https://doi.org/10.1016/j.engfracmech.2021.108227.
- Li, G., Qin, J., Xian, C., Fan, X., Zhang, J., Ding, Y., 2020. Theoretical understandings, key technologies and practices of tight conglomerate oilfield efficient development: a case study of the Mahu oilfield, Junggar Basin, NW China. Petrol. Explor. Dev. 47 (6), 1185–1197. https://doi.org/10.1016/S1876-3804(20)60135-0.
- Li, L., Meng, Q., Wang, S., Li, G., Tang, C., 2013. A numerical investigation of the hydraulic fracturing behaviour of conglomerate in glutenite formation. Acta Geotech 8 (6), 597–618. https://doi.org/10.1007/s11440-013-0209-8.
- Lisjak, A., Mahabadi, O.K., He, L., Tatone, B.S.A., Kaifosh, P., Haque, S.A., Grasselli, G., 2018. Acceleration of a 2D/3D finite-discrete element code for geomechanical simulations using general purpose GPU computing. Comput. Geotech. 100, 84–96. https://doi.org/10.1016/j.compgeo.2018.04.011.
- Liu, J., Ge, H., Mou, S., Wang, X., Wang, J., 2022a. Characterization of meso-structure of glutenite reservoirs by ultrasonic characteristics and the velocity heterogeneity. J. Petrol. Sci. Eng. 208, 109436. https://doi.org/10.1016/ j.petrol.2021.109436.
- Liu, J., Ge, H., Zhang, Z., Wang, X., Wang, J., 2022b. Influence of mechanical contrast between the matrix and gravel on fracture propagation of glutenite. J. Petrol. Sci. Eng. 208, 109639. https://doi.org/10.1016/j.petrol.2021.109639.
- Liu, J., Wang, J., Ge, H., Zhou, W., Chen, B., Li, X., Xue, X., Luo, S., 2023. Effect of gravel on rock failure in glutenite reservoirs under different confining pressures. Petrol. Sci. 20 (5), 3022–3036. https://doi.org/10.1016/j.petsci.2023.04.006.
- Liu, N., Zou, Y., Ma, X., Li, N., Wu, S., 2019. Study of hydraulic fracture growth behavior in heterogeneous tight sandstone formations using CT scanning and acoustic emission monitoring. Petrol. Sci. 16 (2), 396–408. https://doi.org/ 10.1007/s12182-018-0290-6.
- Liu, P., Ju, Y., Ranjith, P.G., Zheng, Z., Chen, J., 2016. Experimental investigation of the effects of heterogeneity and geostress difference on the 3D growth and distribution of hydrofracturing cracks in unconventional reservoir rocks. J. Nat. Gas Sci. Eng. 35, 541–554. https://doi.org/10.1016/j.jngse.2016.08.071.
- Ma, X., Zou, Y., Li, N., Chen, M., Zhang, Y., Liu, Z., 2017. Experimental study on the mechanism of hydraulic fracture growth in a glutenite reservoir. J. Struct. Geol. 97, 37–47. https://doi.org/10.1016/j.jsg.2017.02.012.
- Nie, Y., Zhang, G., Wen, J., Li, S., Zhou, D., 2021. Cyclic injection to reduce hydraulic fracture surface roughness in glutenite reservoirs. Int. J. Rock Mech. Min. Sci. 142, 104740. https://doi.org/10.1016/j.ijrmms.2021.104740.
- Peng, J., Wong, L.N.Y., Teh, C.I., Li, Z., 2018. Modeling micro-cracking behavior of bukit timah granite using grain-based model. Rock Mech. Rock Eng. 51, 135–154. https://doi.org/10.1007/s00603-017-1316-x.

Potyondy, D.O., 2012. A flat-jointed bonded-particle material for hard rock. In: the 46th US Rock Mechanics/Geomechanics Symposium.

- Potyondy, D.O., 2015. The bonded-particle model as a tool for rock mechanics research and application: current trends and future directions. Geosystem Eng. 18 (1), 1–28. https://doi.org/10.1080/12269328.2014.998346.
- Potyondy, D.O., Cundall, P.A., 2004. A bonded-particle model for rock. Int. J. Rock Mech. Min. Sci. 41 (8), 1329–1364. https://doi.org/10.1016/j.ijrmms.2004.09.011.
- Rui, Z., Guo, T., Feng, Q., Qu, Z., Qi, N., Gong, F., 2018. Influence of gravel on the propagation pattern of hydraulic fracture in the glutenite reservoir. J. Petrol. Sci. Eng. 165, 627–639. https://doi.org/10.1016/j.petrol.2018.02.067.
- Shi, X., Qin, Y., Gao, Q., Liu, S., Xu, H., Yu, T., 2023. Experimental study on hydraulic fracture propagation in heterogeneous glutenite rock. Geoenergy Sci. Eng. 225, 211673. https://doi.org/10.1016/j.geoen.2023.211673.
- Shimizu, H., Murata, S., Ishida, T., 2011. The distinct element analysis for hydraulic fracturing in hard rock considering fluid viscosity and particle size distribution. Int. J. Rock Mech. Min. Sci. 48, 712–727. https://doi.org/10.1016/j.jijrmms.2011.04.013.
- Sneddon, I.N., 1946. The distribution of stress in a neighbourhood of a crack in an elastic solid. Proceedings of the Royal Society of London Series A, Mathematical, Physical and Engineering Sciences 187 (1009), 229–260. https://doi.org/ 10.1098/rspa.1946.0077.
- Tang, H., Liang, H., Zhang, L., Qin, J., Li, Y., Zhang, J., 2022. Hydraulic fracture extension patterns of conglomerate reservoirs and relevant influencing factors. Acta Pet. Sin. 43 (6), 871–884. https://doi.org/10.7623/syxb202206011.
- Tang, X., Zhu, H., Zhao, P., Zeng, B., Zhao, M., Dusseault, M.B., McLennan, J.D., 2024.

 A numerical study of complex fractures propagation path in naturally fractured gas shale: reorientation, deflection and convergence. Gas Sci. Eng. 121, 205186. https://doi.org/10.1016/j.igsce.2023.205186.
- https://doi.org/10.1016/j.jgsce.2023.205186.

 Wang, J., Ge, H., Liu, J., Shen, Y., Zhang, Z., Luo, S., Liu, D., 2022. Effects of gravel size and content on the mechanical properties of conglomerate. Rock Mech. Rock Eng. 55 (4), 2493–2502. https://doi.org/10.1007/s00603-021-02760-0.
- Wang, T., Zhang, F., Furtney, J., Damjanac, B., 2022. A review of methods, applications and limitations for incorporating fluid flow in the discrete element method. J. Rock Mech. Geotech. 14 (3), 1005–1024. https://doi.org/10.1016/j.jrmge.2021.10.015.
- Wu, S., Gao, K., Feng, Y., Huang, X., 2022a. Influence of slip and permeability of bedding interface on hydraulic fracturing: a numerical study using combined finite-discrete element method. Comput. Geotech. 148, 104801. https://doi.org/ 10.1016/j.compgeo.2022.104801.
- Wu, S., Ge, H., Li, T., Wang, X., Li, N., Zou, Y., Gao, K., 2022b. Characteristics of fractures stimulated by supercritical carbon dioxide fracturing in shale based on acoustic emission monitoring. Int. J. Rock Mech. Min. Sci. 152, 105065. https:// doi.org/10.1016/j.ijrmms.2022.105065.
- Yoon, J.S., Zang, A., Stephansson, O., 2014. Numerical investigation on optimized stimulation of intact and naturally fractured deep geothermal reservoirs using hydro-mechanical coupled discrete particles joints model. Geothermics 52, 165–184. https://doi.org/10.1016/j.geothermics.2014.01.009.
- Yoon, J.S., Zimmermann, G., Zang, A., 2015a. Numerical investigation on stress shadowing in fluid injection - induced fracture propagation in naturally fractured geothermal reservoirs. Rock Mech. Rock Eng. 48 (4), 1439–1454. https:// doi.org/10.1007/s00603-014-0695-5.
- Yoon, J.S., Zimmermann, G., Zang, A., 2015b. Discrete element modeling of cyclic rate fluid injection at multiple locations in naturally fractured reservoirs. Int. J. Rock Mech. Min. Sci. 74, 15–23. https://doi.org/10.1016/j.ijrmms.2014.12.003.
- Yu, T., Yuan, F., Zhou, P., Hao, L., Zou, Y., Ma, X., Zhang, Z., 2021. Fracture propagating shapes in gravel-supported conglomerate reservoirs of upper wuerhe formation on manan slope, Mahu sag. Xinjing Pet. Geol. 42 (1), 53–62. https:// doi.org/10.7657/XJPG20210607.
- Yu, S., Zhou, Y., Yang, J., Chen, W., 2023. Hydraulic fracturing modelling of glutenite formations using an improved form of SPH method. Geoenergy Sci. Eng. 227, 211842. https://doi.org/10.1016/j.geoen.2023.211842.
- Zang, C., Jiang, H., Shi, S., Li, J., Zou, Y., Zhang, S., Tian, G., Yang, P., 2022. An analysis of the uniformity of multi-fracture initiation based on downhole video imaging technology: a case study of Mahu tight conglomerate in Junggar Basin, NW China. Petrol. Explor. Dev. 49 (2), 2703–2722. https://doi.org/10.1016/S1876-3804(22)60038-7.
- Zhang, F., Damjanac, B., Huang, H., 2013. Coupled discrete element modeling of fluid injection into dense granular media. J. Geophys. Res. Solid Earth 118, B06302. https://doi.org/10.1002/jgrb.50204.
- Zhang, G., Sun, S., Chao, K., Niu, R., Liu, B., Li, Y., Wang, F., 2019. Investigation of the nucleation, propagation and coalescence of hydraulic fractures in glutenite reservoirs using a coupled fluid flow-DEM approach. Powder Technol. 354, 301–313. https://doi.org/10.1016/j.powtec.2019.05.073.
- Zhang, Y., Wong, L.N.Y., 2018. A review of numerical techniques approaching microstructures of crystalline rocks. Comput. Geosci. 115, 167–187. https://doi.org/ 10.1016/j.cageo.2018.03.012.
- Zhang, Z., Zhang, S., Shi, S., Zou, Y., Li, J., Ma, X., Xiao, F., 2022. Evaluation of multiscale mechanical properties of conglomerate using nanoindentation and homogenization methods: a case study on tight conglomerate reservoirs in southern slope of Mahu sag. Chin. J. Rock Mech. Eng. 41 (5), 926—940. https://

doi.org/10.13722/j.cnki.jrme.2021.1186.

- Zhang, Z., Ge, H., Wang, J., Liu, J., Liu, D., Teng, W., Shen, Y., 2023. Influence of gravel content and cement on conglomerate fracture. Petrol. Sci. 20 (3), 1724–1741. https://doi.org/10.1016/j.petsci.2023.03.027.
- Zhao, P., Xie, L., Fan, Z., Deng, L., Liu, J., 2021. Mutual interference of layer plane and natural fracture in the failure behavior of shale and the mechanism investigation. Petrol Sci. 18 (2), 618–640. https://doi.org/10.1007/s12182-020-00510-5
- tion. Petrol. Sci. 18 (2), 618–640. https://doi.org/10.1007/s12182-020-00510-5. Zhou, J., Lan, H., Zhang, L., Yang, D., Song, J., Wang, S., 2019. Novel grain-based model for simulation of brittle failure of Alxa porphyritic granite. Eng. Geol. 251, 100–114. https://doi.org/10.1016/j.enggeo.2019.02.005.
- Zhu, H., Huang, C., Tang, X., McLennan, J.D., 2023. Multicluster fractures propagation during temporary plugging fracturing in naturally fractured reservoirs integrated with dynamic perforation erosion. SPE J. 28 (4), 1986–2002. https://doi.org/10.2118/214666-PA.
- Zou, Y., Shi, S., Zhang, S., Yu, T., Tian, G., Ma, X., Zhang, Z., 2021. Experimental modeling of sanding fracturing and conductivity of propped fractures in conglomerate: a case study of tight conglomerate of Mahu sag in Junggar Basin, NW China. Petrol. Explor. Dev. 48 (6), 1202–1209. https://doi.org/10.1016/S1876-3804(21)60294-X.